

Magnetic acceleration of ultra-relativistic jets in gamma-ray burst sources

Serguei S. Komissarov,^{1*} Nektarios Vlahakis,^{2*} ArieH Königl^{3*} and Maxim V. Barkov,^{1,4*}

¹*Department of Applied Mathematics, The University of Leeds, Leeds, LS2 9GT*

²*Section of Astrophysics, Astronomy and Mechanics, Physics Department, University of Athens, 15784 Zografos, Athens, Greece*

³*Department of Astronomy and Astrophysics and Enrico Fermi Institute, University of Chicago, 5640 South Ellis Avenue, Chicago, IL 60637, USA*

⁴*Space Research Institute, 84/32 Profsoyuznaya Street, Moscow 117997, Russia*

Received/Accepted

ABSTRACT

We present numerical simulations of axisymmetric, magnetically driven outflows that reproduce the inferred properties of ultra-relativistic gamma-ray burst (GRB) jets. These results extend our previous simulations (Komissarov et al. 2007) of outflows accelerated to moderately relativistic speeds, which we applied to jets of active galactic nuclei. In contrast to several recent investigations, which have employed the magnetodynamics approximation, our numerical scheme solves the full set of equations of special-relativistic, ideal MHD, which enables us to explicitly calculate the jet velocity and magnetic-to-kinetic energy conversion efficiency — key parameters of interest for astrophysical applications. We confirm that the magnetic acceleration scheme remains robust into the ultra-relativistic regime, as previously indicated by semi-analytic self-similar solutions. We find that all current-carrying outflows exhibit self-collimation and consequent acceleration near the rotation axis, but that unconfined outflows lose causal connectivity across the jet and therefore do not collimate or accelerate efficiently in their outer regions. We show that magnetically accelerated jets confined by an external pressure that varies as $z^{-\alpha}$ ($0 < \alpha \leq 2$) assume a paraboloidal shape $z \propto r^a$ (where r, z are cylindrical coordinates and $a > 1$), and we obtain analytic expressions for the one-to-one correspondence between the pressure distribution and the asymptotic jet shape. We demonstrate that the acceleration efficiency of jets with paraboloidal streamlines is $\gtrsim 50\%$, with the numerical value being higher the lower the initial magnetization. We derive asymptotic analytic expressions for the acceleration of initially cold outflows along paraboloidal streamlines and verify that they provide good descriptions of the simulated flows. Our modelled jets (corresponding to $3/2 < a < 3$) attain Lorentz factors $\Gamma \gtrsim 10^2$ on scales $\sim 10^{10} - 10^{12}$ cm, consistent with the possibility that long/soft GRB jets are accelerated within envelopes of collapsing massive stars, and $\Gamma \gtrsim 30$ on scales $\sim 9 \times 10^8 - 3 \times 10^{10}$ cm, consistent with the possibility that short/hard GRB jets are accelerated on scales where they can be confined by moderately relativistic winds from accretion discs. We also find that $\Gamma\theta_v \sim 1$ for magnetically accelerated jets, where θ_v is the half-opening angle of the poloidal streamlines, which implies that the γ -ray emitting components of GRB outflows are very narrow, with $\theta_v \lesssim 1^\circ$ in regions where $\Gamma \gtrsim 100$, and that the afterglow light curves of these components would either exhibit a very early jet break or show no jet break at all.

Key words: MHD – relativity – methods: numerical – gamma-rays: bursts

1 INTRODUCTION

In the “standard” model of long-duration, soft-spectrum gamma-ray bursts (GRBs; e.g. Piran 2005), the prompt high-energy emission arises in ultra-relativistic (bulk

* E-Mail: serguei@maths.leeds.ac.uk (SSK); vlahakis@phys.uoa.gr (NV); arieh@jets.uchicago.edu (AK); bmv@maths.leeds.ac.uk (MVB)

Lorentz factor $\Gamma \gtrsim 10^2$), highly collimated (opening half-angle of a few degrees) jets. The high Lorentz factors are inferred from the requirement of a sufficiently low opacity to photon-photon annihilation or to scattering by photon annihilation-produced electron-positron pairs (e.g. Lithwick & Sari 2001), whereas the jet opening angle is deduced from the detection of a panchromatic break in the light curve of the lower-energy afterglow emission (e.g. Rhoads 1999; Sari et al. 1999). Recent observations by the *Swift* satellite have indicated that various aspects of this model may need to be modified (e.g. Mészáros 2006; Panaitescu 2007; Liang et al. 2008), but the basic picture of a collimated $\Gamma \gtrsim 10^2$ outflow is still the accepted paradigm.

Observations of long/soft GRBs and their afterglows have revealed that these events typically involve the release of a few times 10^{51} erg, although the fraction of this energy that corresponds to the γ -ray emitting outflow component may vary from source to source (e.g. Berger et al. 2003a; Frail et al. 2005). The outflows in these GRBs have been argued to originate either in a magnetar or in a rapidly accreting stellar-mass black hole, formed in the collapse of a massive star. The jets could tap into the rotational energy of the neutron star, black hole or accretion disc through the agency of an ordered magnetic field that threads the source (e.g. Usov 1992; Thompson 1994; Mészáros & Rees 1997; Katz 1997; Kluźniak & Ruderman 1998; Vlahakis & Königl 2001, 2003a,b; Blandford 2002; Drenkhahn & Spruit 2002; Vlahakis et al. 2003; Proga et al. 2003; McKinney 2006; Lyutikov 2006b; Levinson 2006; Komissarov & Barkov 2007; Bucciantini et al. 2008; Barkov & Komissarov 2008). For typical burst energies and durations the field amplitudes should be $\sim 10^{14} - 10^{15}$ G. Early models have postulated that GRB outflows are driven purely thermally via annihilation of neutrinos emitted by the accretion disc. Although this model remains very popular, some recent studies have indicated that the neutrino heating may not be as efficient as previously thought (e.g. Di Matteo et al. 2002). At present, both the magnetic and the thermal mechanisms seem equally possible and it may well be that in many cases they operate simultaneously. In particular, neutrino heating may play an important role in the initial acceleration of magnetized outflows (e.g. Vlahakis & Königl 2003a) and in determining their mass load (e.g. Levinson 2006; Barzilay & Levinson 2008).

While short/hard GRBs evidently have different progenitors (quite possibly merging neutron stars or neutron star/black hole pairs) and on average involve a smaller energy release, a lower Lorentz factor, and weaker collimation than long/soft GRBs, they may well represent the same basic phenomenon and arise in relativistic outflows that are driven in a similar way (e.g. Nakar 2007).

The magnetic acceleration and collimation of GRB outflows needs to be studied within the framework of relativistic magnetohydrodynamics (MHD). Although general-relativistic effects may influence the conditions near the base of the flow, most of the action takes place sufficiently far away from the central mass that the simpler equations of special-relativistic MHD can be employed. Since our focus in this paper is on the global structure of GRB jets, we henceforth consider only the special-relativistic theory. However, even in this case there are qualitatively new effects in comparison with Newtonian MHD. These include the fact

that, when the bulk Lorentz factor becomes large, the electric force can no longer be neglected relative to the magnetic force and, in fact, becomes comparable to it in magnitude. Correspondingly, one needs to retain the displacement current and the electric charge density in Maxwell’s equations. Another consequence of relativistic motion (which also affects unmagnetized flows) is the coupling between different spatial components of the momentum conservation equation brought about by the appearance of the Lorentz factor (which is calculated from the total velocity) in each of the component equations. Furthermore, in cases where the temperature (i.e. the characteristic velocity of internal motions) is relativistic, one needs to take into account the enthalpy contribution to the inertia of the flow. On account of these various factors, relativistic MHD does not naturally yield simple generalizations of results obtained in Newtonian MHD. To simplify the treatment, various authors have adopted the force-free electrodynamics (also termed “magnetodynamics”) approximation, in which the matter inertia is neglected altogether. While this approach has led to useful insights and interesting exact solutions, it is inherently limited in that one cannot explicitly calculate the fluid velocity and hence the efficiency of transforming electromagnetic energy into kinetic form, which are key parameters of interest for astrophysical applications.

In a pioneering work, Li et al. (1992; see also Contopoulos 1994) derived exact semi-analytic MHD solutions of steady, axisymmetric, “cold” relativistic flows patterned after the Newtonian radially self-similar outflow solutions of Blandford & Payne (1982). In contrast with the Newtonian solutions, one cannot match the flow in the relativistic case to a given power-law radial distribution of the rotation velocity of the source (e.g. the $\propto r^{-1/2}$ rotation law of a Keplerian accretion disc) because the relativistic equations already contain the (constant) speed of light c . However, this constraint only affects the base of the flow (and, as shown by Vlahakis & Königl 2003a, it is possible to approximate a Keplerian disc even in this case by judiciously parametrizing the disc height above the origin of the coordinate system), and one can proceed to obtain the global structure of the outflow as in the Newtonian case. Li et al. (1992) identified as a key property of the relativistic outflow solutions the spatially extended nature of the acceleration region, which continues well beyond the classical fast-magnetosonic surface. These results were further generalized to initially “hot” outflows by Vlahakis & Königl (2003a,b), who went on to apply the relativistic self-similar solutions to GRB outflows (see also Vlahakis & Königl 2001 and Vlahakis et al. 2003) and to the lower- Γ jets imaged in active galactic nuclei (AGNs; Vlahakis & Königl 2004). The solutions obtained in these papers confirmed that spatially extended acceleration is a generic property of MHD outflows that distinguishes it from purely hydrodynamic, thermally driven winds. Vlahakis & Königl (2001, 2003a) noted that this property can be understood from the fact that the magnetic acceleration is determined from the joint solution of the Bernoulli equation (derived from the momentum conservation equation along the poloidal magnetic field) and the trans-field equation (which describes the force balance in the transverse direction). The effective singular surface (the “event horizon” for the propagation of fast-magnetosonic waves) is the so-called modified fast magnetosonic surface, which

can lie well beyond the corresponding classical surface. (The classical fast-magnetosonic surface is singular only when one solves the Bernoulli equation alone, assuming that the shape of the field lines is given; in Section 5 we further elaborate on the strong connection between acceleration and poloidal field-line shape in magnetically driven flows.)

The semi-analytic solutions have also established the collimation properties of MHD outflows, demonstrating that they converge asymptotically to cylinders for flows that are Poynting flux-dominated at the source and to cones when the enthalpy flux is initially dominant (e.g. Vlahakis & Königl 2003a,b). These solutions are, however, limited by the self-similarity assumption, which, besides restricting the angular velocity distribution at their base, also requires the magnetic flux distribution to be a power law in radius and only enables one current regime (current-carrying or return-current, but not a global current circuit) to be modelled by any given solution. To validate the applicability of these results under more realistic circumstances and to ascertain their dynamical stability, one needs to resort to numerical simulations. However, the large spatial extent of the acceleration region (which, according to the semi-analytic solutions, typically covers several decades in spherical radius) has posed a strong challenge for such calculations: in fact, early attempts to simulate such flows were limited by numerical dissipation to maximum Lorentz factors that were only a small fraction (less than 1%) of the potentially achievable terminal value.

Komissarov et al. (2007; hereafter Paper I) have taken a major step toward overcoming this challenge by employing a special-relativistic, ideal-MHD numerical scheme that was specifically designed to optimize accuracy and resolution and to minimize numerical dissipation. A key element of their approach was the implementation of a grid-extension method that made it possible to follow the flow up to six decades in spatial scale while reducing the computation time by up to three orders of magnitude. They were able to model cold flows that converted nearly 80% of the initial Poynting flux into kinetic energy of $\Gamma_\infty \gtrsim 10$ baryons and demonstrated that the results were consistent with the available data on the acceleration of relativistic jets in AGNs. They found that the numerical solutions assumed a quasi-static configuration that was qualitatively in accord with the self-similar AGN jet models of Vlahakis & Königl (2004). The simulations were, however, able to examine various aspects of the flow that could not be studied within the framework of a self-similar model (including the structure of outflows in which both the current and the return current flow within the jet and the dependence of the collimation properties on the shape of the jet boundary) and uncovered new features (such as the formation of a cylindrical core around the jet axis) that were inherently non-self-similar.

In this paper we further extend the scheme presented in Paper I to cover the regime of GRB outflows. In particular, we present simulations of outflows that attain terminal Lorentz factors $\Gamma_\infty \gtrsim 10^2$, following them over up to eight decades in axial scale. Besides cold jets, we also consider the case of an outflow in which the enthalpy flux is a significant fraction of the injected energy flux. Owing to the larger range in Γ in comparison with the solutions presented in Paper I, the magnetic acceleration region can now be better isolated, which enables us to more accurately compare

its behaviour with that of the self-similar solutions and to analyse it using the asymptotic forms of the Bernoulli and trans-field equations. We begin by reviewing the relativistic MHD formalism (Section 2) and our numerical scheme (Section 3). We present key simulation results in Section 4 and discuss them in the context of the theory of magnetic acceleration in Section 5. Section 6 deals with applications of our results to GRBs. Our conclusions are given in Section 7.

2 BASIC EQUATIONS

Since most of the acceleration takes place far away from the source, we assume that the space-time is flat. In an inertial frame at rest relative to the source, the relativistic ideal-MHD equations that describe the flow take the following form: *continuity equation*

$$(1/c)\partial_t(\sqrt{-g}\rho u^t) + \partial_i(\sqrt{-g}\rho u^i) = 0, \quad (1)$$

where ρ is the rest mass density of matter, u^ν is its 4-velocity, and g is the determinant of the metric tensor; *energy-momentum equations*

$$(1/c)\partial_t(\sqrt{-g}T^\nu{}_\nu) + \partial_i(\sqrt{-g}T^\nu{}_i) = \frac{\sqrt{-g}}{2}\partial_\nu(g_{\alpha\beta})T^{\alpha\beta}, \quad (2)$$

where $T^{\kappa\nu}$ is the total stress-energy-momentum tensor; *induction equation*

$$(1/c)\partial_t(B^i) + e^{ijk}\partial_j(E_k) = 0, \quad (3)$$

where $e_{ijk} = \sqrt{\gamma}\epsilon_{ijk}$ is the Levi-Civita tensor of the absolute space ($\epsilon_{123} = 1$ for right-handed systems and $\epsilon_{123} = -1$ for left-handed ones) and γ is the determinant of the spatial part of the metric tensor ($\gamma_{ij} = g_{ij}$); *solenoidal condition*

$$\partial_i(\sqrt{\gamma}B^i) = 0. \quad (4)$$

The total stress-energy-momentum tensor, $T^{\kappa\nu}$, is a sum of the stress-energy momentum tensor of matter,

$$T_{(m)}^{\kappa\nu} = wu^\kappa u^\nu / c^2 + pg^{\kappa\nu}, \quad (5)$$

where p is the thermodynamic pressure and w is the enthalpy per unit volume, and the stress-energy momentum tensor of the electromagnetic field,

$$T_{(e)}^{\kappa\nu} = \frac{1}{4\pi} \left[F^{\kappa\alpha} F^\nu{}_\alpha - \frac{1}{4}(F^{\alpha\beta} F_{\alpha\beta})g^{\kappa\nu} \right], \quad (6)$$

where $F^{\nu\kappa}$ is the Maxwell tensor. The electric and magnetic fields are defined as measured by an observer stationary relative to the spatial grid, which gives

$$B^i = \frac{1}{2}e^{ijk}F_{jk} \quad (7)$$

and

$$E_i = F_{it}. \quad (8)$$

In the limit of ideal MHD

$$E_i = -e_{ijk}v^j B^k / c, \quad (9)$$

where $v^i = u^i / u^t$ is the usual 3-velocity of the plasma.

In all of our simulations we use an isentropic equation of state

$$p = Q\rho^s, \quad (10)$$

where $Q = \text{const}$ and $s = 4/3$. This relation enables us to exclude the energy equation from the integrated system. However, the momentum equation remains intact, including the non-linear advection term. Therefore, if the conditions for shock formation were to arise, our calculation would capture that shock.¹ The enthalpy per unit volume is

$$w = \rho c^2 + \frac{s}{s-1} p. \quad (11)$$

2.1 Field-line constants

The poloidal magnetic field is fully described by the azimuthal component of the vector potential,

$$B^i = \frac{1}{\sqrt{\gamma}} \epsilon^{ij\phi} \frac{\partial A_\phi}{\partial x^j}. \quad (12)$$

For axisymmetric solutions $A_\phi = \Psi/2\pi$, where $\Psi(x^i)$, the so-called magnetic flux function, is the total magnetic flux enclosed by the circle $x^i = \text{const}$ (x^i being the coordinates of the meridional plane). Stationary and axisymmetric ideal MHD flows have five quantities that propagate unchanged along the magnetic field lines and thus are functions of Ψ alone. These are k , the mass flux per unit magnetic flux; Ω , the angular velocity of magnetic field lines; l , the total angular momentum flux per unit rest-mass flux; μ , the total energy flux per unit rest-mass energy flux; and Q , the entropy per particle:

$$k = \frac{\rho u_p}{B_p}, \quad (13)$$

$$\Omega = \frac{v^\phi}{r} - \frac{v_p}{r} \frac{B^\phi}{B_p}, \quad (14)$$

$$l = -\frac{I}{2\pi k c} + r \frac{w}{\rho c^2} \Gamma v^\phi, \quad (15)$$

$$\mu = \mu_h + \mu_m, \quad (16)$$

and

$$Q = P/\rho^s, \quad (17)$$

where $u_p = \Gamma v_p$ is the magnitude of the poloidal component of the 4-velocity, B_p is the magnitude of the poloidal component of the magnetic field, r is the cylindrical radius,

$$I = \frac{c}{2} r B^\phi \quad (18)$$

is the total electric current flowing through a loop of radius r around the rotation axis,

$$\mu_h = \frac{w}{\rho c^2} \Gamma \quad (19)$$

is the total hydrodynamic energy (rest mass plus thermal plus kinetic) flux per unit rest-mass energy flux,

$$\mu_m = \mu_h \sigma = -\frac{\Omega I}{2\pi k c^3} \quad (20)$$

¹ Since entropy is fixed, the compression of our shocks would be the same as for continuous compression waves. This would give a higher jump in density for the same jump in pressure than in a proper (dissipative) shock. Fortunately, we do not need to contend with this issue in practice as shocks do not form in our simulations.

is the Poynting flux per unit rest-mass energy flux, and σ is the ratio of the Poynting flux to the hydrodynamic (rest-mass plus thermal plus kinetic) energy flux. For cold flows $Q = 0$, $w = \rho c^2$. (Here and in the rest of the paper we use a hat symbol over vector indices to indicate their components in a normalized coordinate basis.) From equation (16) it follows that the Lorentz factor Γ cannot exceed μ .

3 NUMERICAL SIMULATIONS

To maintain a firm control over the jet's confinement and to prevent complications related to numerical diffusion of the denser plasma from the jet's surroundings, we study outflows that propagate inside a solid funnel of a prescribed shape.² Specifically, we consider axisymmetric funnels

$$z \propto r^a,$$

where z and r are the cylindrical coordinates of the funnel wall and $a = 2/3, 1, 3/2, 2$ and 3 . We employ elliptical coordinates $\{\xi, \eta, \phi\}$, where

$$\xi = r z^{-1/a} \quad (21)$$

and

$$\eta^2 = \frac{r^2}{a} + z^2 \quad (22)$$

(see Paper I for details).

We use a Godunov-type numerical code based on the scheme described in Komissarov (1999a). To reduce numerical diffusion we apply parabolic reconstruction instead of the linear one of the original code. Our procedure, in brief, is to calculate minmod-averaged first and second derivatives and use the first three terms of the Taylor expansion for spatial reconstruction. This simple procedure results in a noticeable improvement in the solution accuracy even though the new scheme is still not 3rd-order accurate because of the non-uniformity of the grid.

The grid is uniform in the ξ direction (the polar angle direction when we use spherical coordinates), where in most runs it has a total of 60 cells. To check the convergence, some runs were repeated with a doubled resolution. The cells are elongated in the η direction (the radial direction when we use spherical coordinates), reflecting the elongation of the funnel. Very elongated cells lead to a numerical instability, so we imposed an upper limit of 40 on the length/width ratio.

To speed up the simulations, we implement a sectioning of the computational grid as described in Komissarov & Lyubarsky (2004). In each section, which is shaped as a ring, the numerical solution is advanced using a time step based on the local Courant condition. It is twice as large as the time step of the adjacent inner ring and twice as small as the time step of the adjacent outer ring. This approach is particularly effective for conical flows but less so for highly collimated, almost cylindrical configurations.

² As was already noted in Paper I, in real astrophysical systems the shape of the boundary is determined by the spatial distribution of the pressure or the density of the confining ambient medium. The effective ambient pressure distributions implied by the adopted funnel shapes are considered in Section 5.3.

The equations are dimensionalized in the following manner. The unit of length, L , is such that $\eta_i = 1$, where the subscript i refers to the inlet boundary. The unit of time is $T = L/c$. The unit of mass is $M = L^3 B_0^2 / 4\pi c^2$, where B_0 is the dimensional magnitude of the η component of magnetic field at the inlet (so the dimensionless magnitude of $B^{\hat{\eta}}$ at the inlet is $\sqrt{4\pi}$). In applications, L is the typical length-scale of the launch region, T is the light crossing time of that region and B_0 is the typical strength of the poloidal magnetic field at the origin. Notice that L does not have to be the size of the rotating object at the base of the jet and in particular it cannot be identified with the radius of the black hole event horizon which allows only inflows. When dimensional estimates are required we use the expected magnitude of the light-cylinder radius, $r_{1c} \equiv c/\Omega$. The mass scale M does not represent the mass of the central object but rather the rest-mass equivalent of the magnetic energy within the magnetosphere.

3.1 Boundary conditions

3.1.1 Inlet boundary

We treat the inlet boundary, $\eta_i = 1$, as a surface of a perfectly conducting rotator with either a uniform angular velocity $\Omega = \Omega_0$ or with

$$\Omega = \Omega_0(1 + a_2(\xi/\xi_j)^2 + a_3(\xi/\xi_j)^3), \quad (23)$$

where the subscript j refers to the jet boundary (funnel wall). In this paper we set $a_2 = 0.778$ and $a_3 = -1.778$. The angular velocity profile is directly related to the distribution of the electric current in the jet, which for $r \gg r_{1c}$ is given by

$$I \approx -\frac{1}{2}\Omega B_p r^2 \quad (24)$$

(see Paper I, or equation 34 in Section 5.2). In fact, the current is driven by the electric field associated with the rotating poloidal field, and the electric charge conservation requires the circuit to eventually close. In the case of a constant Ω the return current flows over the jet boundary, whereas in the case of differential rotation with $\Omega(\xi_j) = 0$ it flows mainly inside the jet (within $0.75 < \xi/\xi_j < 1$ for the Ω distribution given by equation 23). The solid-body rotation law provides a very good description of the behaviour of magnetic field lines that thread the horizon of a black hole or the surface of a magnetized star. This choice is therefore entirely appropriate for the black-hole or magnetar theory of GRB jets. On the other hand, differential rotation is a natural choice for jets that are launched from an accretion disc, and although the distribution (23) does not correspond to a realistic disc model, it should nevertheless capture the qualitative aspects of such a system.³

The condition of perfect conductivity allows us to fix the azimuthal component of the electric field and the η component of the magnetic field:

$$E_\phi = 0, \quad B^{\hat{\eta}} = B_0 \quad \text{at} \quad \eta = \eta_i. \quad (25)$$

From the first of these conditions we derive

$$v^{\hat{\xi}} = \frac{v^{\hat{\eta}}}{B^{\hat{\eta}}} B^{\hat{\xi}} \quad (26)$$

and (using equation 14)

$$v^{\hat{\phi}} = r\Omega + \frac{v^{\hat{\eta}}}{B^{\hat{\eta}}} B^{\hat{\phi}}. \quad (27)$$

The adopted uniform distribution of $B^{\hat{\eta}}$ is consistent with transverse mechanical equilibrium at the inlet. We have also experimented with nonuniform distributions of the magnetic field, in particular with $B^{\hat{\eta}}$ decreasing with ξ . The results were not significantly different as the field distribution downstream of the inlet underwent a rapid rearrangement that restored the transverse force balance.

To have control over the mass flux, the flow at the inlet boundary is set to be super-slow-magnetosonic. This means that both the density and the radial component of the velocity can be prescribed some fixed values:

$$\rho = \rho_0, \quad v^{\hat{\eta}} = v_{p0}.$$

In the simulations we use $v_{p0} = 0.5c$ or $0.7c$, which is a choice of convenience. On the one hand, this value is sufficiently small to insure that the flow at $\eta_i = 1$ is sub-Alfvénic and hence that the Alfvén and fast-magnetosonic critical surfaces are located downstream of the inlet boundary. On the other hand, it is large enough to promote the rapid establishment of a steady state (in which the outflow speed remains constant along the symmetry axis). Because of the sub-Alfvénic nature of the inlet flow, we cannot fix the other components of the magnetic field and the velocity — they are to be found as part of the global solution. Following the standard approach we extrapolate $B^{\hat{\phi}}$ and $B^{\hat{\xi}}$ from the domain into the inlet boundary cells. We then compute $v^{\hat{\phi}}$ and $v^{\hat{\xi}}$ from equations (26) and (27).

The magnitude of the angular velocity is chosen in such a way that the Alfvén surface is encountered close to the source. Specifically, in the case of solid-body rotation the light cylinder radius, r_{1c} , is $\simeq 50\%$ larger than the initial jet radius. In the differential rotation case, the closest point of the Alfvén surface is located at a distance of $\simeq 1$ initial jet radius from the inlet surface.

The inlet density varies from model to model in order to cover a wide range of initial magnetizations. Table I gives the key parameters of all the jet models constructed in this study. Most of the models, denoted by the letter B, correspond to the wall shape $z \propto r^{3/2}$ and differ only by the value of the magnetization parameter: μ varies from the relatively small value of 39, which is more suitable to AGN jets (see Paper I), all the way up to 620. Model B2H is included to study the effects of a high temperature at the source. The initial effective thermal Lorentz factor in this model is $\Gamma_{t0} = w_0/\rho_0 c^2 = 55$. Models A and AW have a wall of conical shape. In model AW the half-opening angle of the cone is 90° , which allows us to model the case of an unconfined outflow (which could be relevant to pulsar winds). The remaining models help to explore the effects of differential rotation (model D), of various other paraboloidal wall shapes ($z \propto r^2$ in model C, $z \propto r^3$ in model F) and of a wall shape whose opening angle increases with distance (model E).

³ Note in this connection that Tchekhovskoy et al. (2008) simulated a force-free black-hole/disc outflow in which current flowed out along field lines that threaded the uniformly rotating hole and returned along field lines attached to the differentially rotating disc.

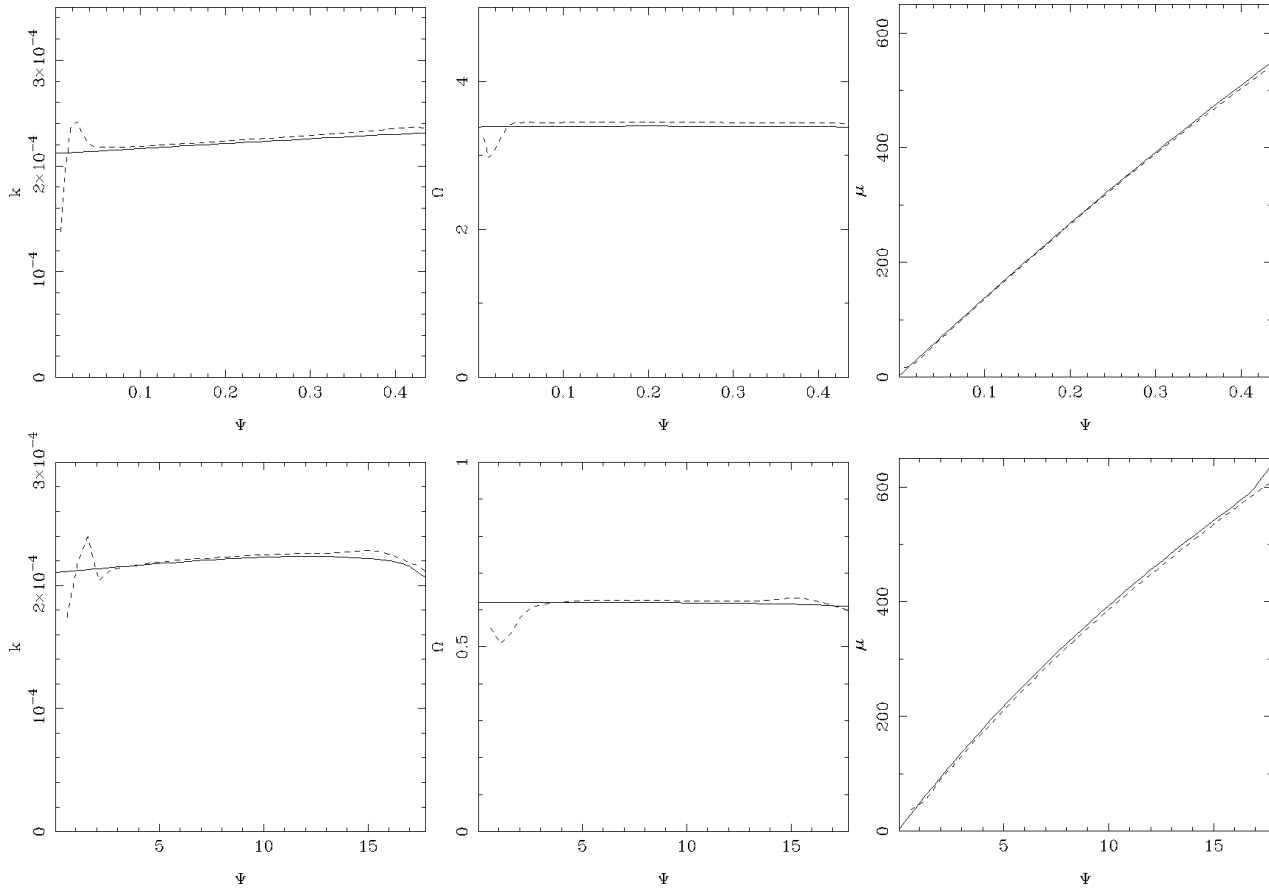


Figure 1. Computational errors for models A (top row) and B1 (bottom row). The plots show the flow parameters $k(\Psi)$, $\Omega(\Psi)$ and $\mu(\Psi)$ at the inlet (solid lines) and at $\eta = 1 \times 10^5$ for model A and $\eta = 5 \times 10^7$ for model B1 (dashed lines).

Table 1. Parameters of simulation models.

Model	a	rotation	$w_0/\rho_0 c^2$	ξ_j or θ_j	μ_{\max}
A	1	uniform	1.0	$\theta_j = 0.2$	560
AW	1	uniform	1.0	$\theta_j = \pi/2$	560
B1	3/2	uniform	1.0	$\xi_j = 2.0$	620
B2	3/2	uniform	1.0	$\xi_j = 2.0$	310
B2H	3/2	uniform	55	$\xi_j = 2.0$	370
B3	3/2	uniform	1.0	$\xi_j = 2.0$	155
B4	3/2	uniform	1.0	$\xi_j = 2.0$	78
B5	3/2	uniform	1.0	$\xi_j = 2.0$	39
C	2	uniform	1.0	$\xi_j = 2.0$	620
D	3/2	differential	1.0	$\xi_j = 2.0$	600
E	2/3	uniform	1.0	$\xi_j = 0.1$	300
F	3.0	uniform	1.0	$\xi_j = 2.0$	540

3.1.2 Other boundaries

The computational domain is always chosen to be long enough for the jet to be super-fast-magnetosonic when it approaches the outlet boundary $\eta = \eta_0$. This justifies the

use of radiative boundary conditions at this boundary (i.e. we determine the state variables of the boundary cells via extrapolation of the domain solution).

At the polar axis, $\xi = 0$, we impose symmetry boundary conditions for the dependent variables that are expected to pass through zero there,

$$f(-\xi) = -f(\xi).$$

These variables include $B^{\hat{\xi}}$, $B^{\hat{\phi}}$, $u^{\hat{\xi}}$ and $u^{\hat{\phi}}$. For other variables we impose a “zero second derivative” condition,

$$\partial^2 f / \partial \xi^2 = 0,$$

which means that we use linear interpolation to calculate the values of these variables in the boundary cells.

We do this in order to improve the numerical representation of a narrow core that develops in all cases as a result of the magnetic hoop stress. Within this core the gradients in the ξ direction are very large and the usual zero-gradient condition, $f(-\xi) = f(\xi)$, results in increased numerical diffusion in this region. We have checked that this has a noticeable effect only on the axial region and that the global solution does not depend on which of these two conditions is used.

At the wall boundary, $\xi = \xi_j$, we use a reflection condition,

$$f(\xi_j + \Delta\xi) = -f(\xi_j - \Delta\xi),$$

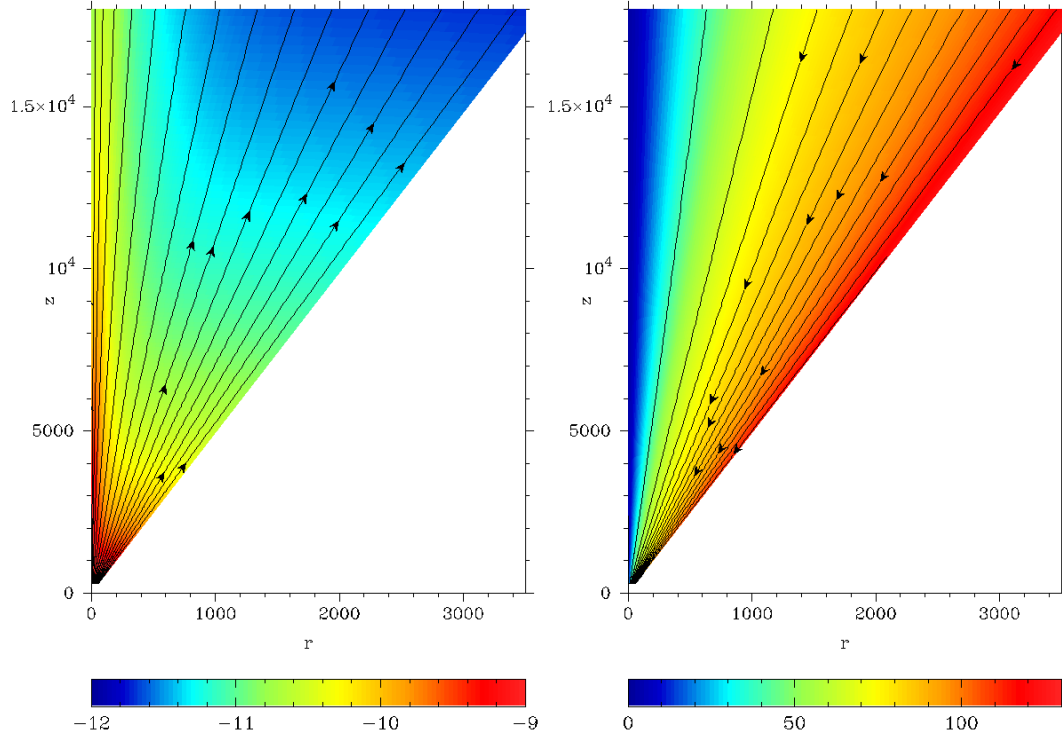


Figure 2. Model A. Left panel shows $\log_{10} \rho'$ (colour), where $\rho' = \Gamma\rho$ is the jet density as measured in the frame of jet source, and the magnetic field lines. Right panel shows the Lorentz factor (colour) and the current lines. The light cylinder radius is $r_{lc} = 0.29$.

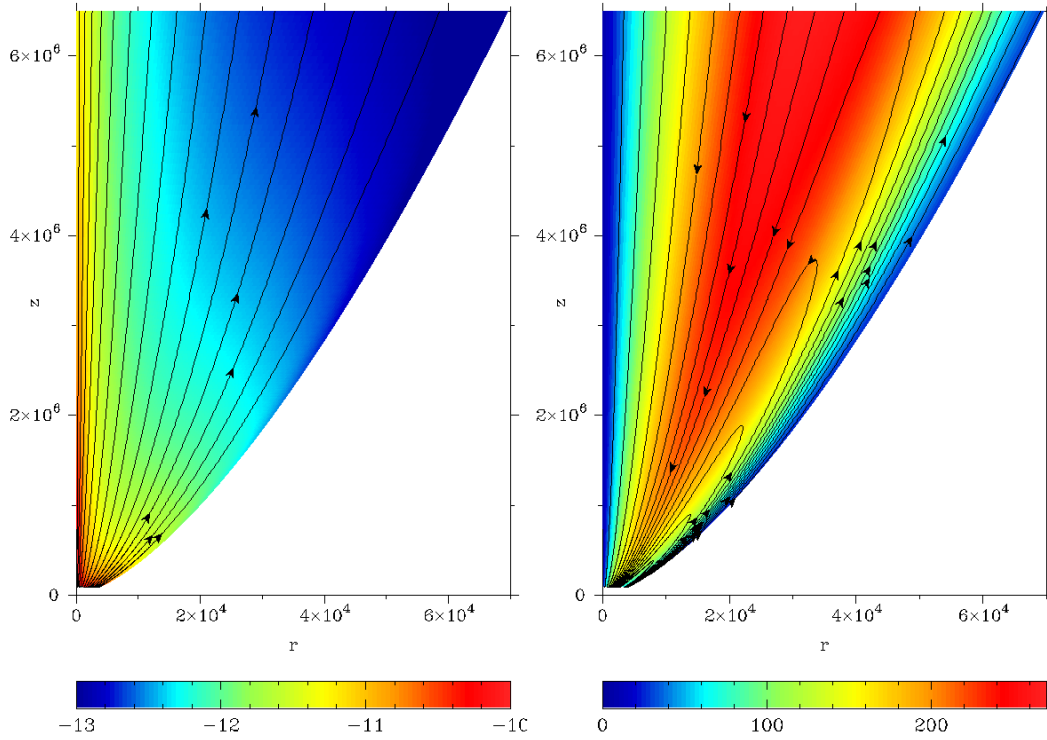


Figure 3. Same as in Fig. 2, but for model D. The closest to the inlet point of the Alfvén surface has the radius $r_{lc} = 1.3$.

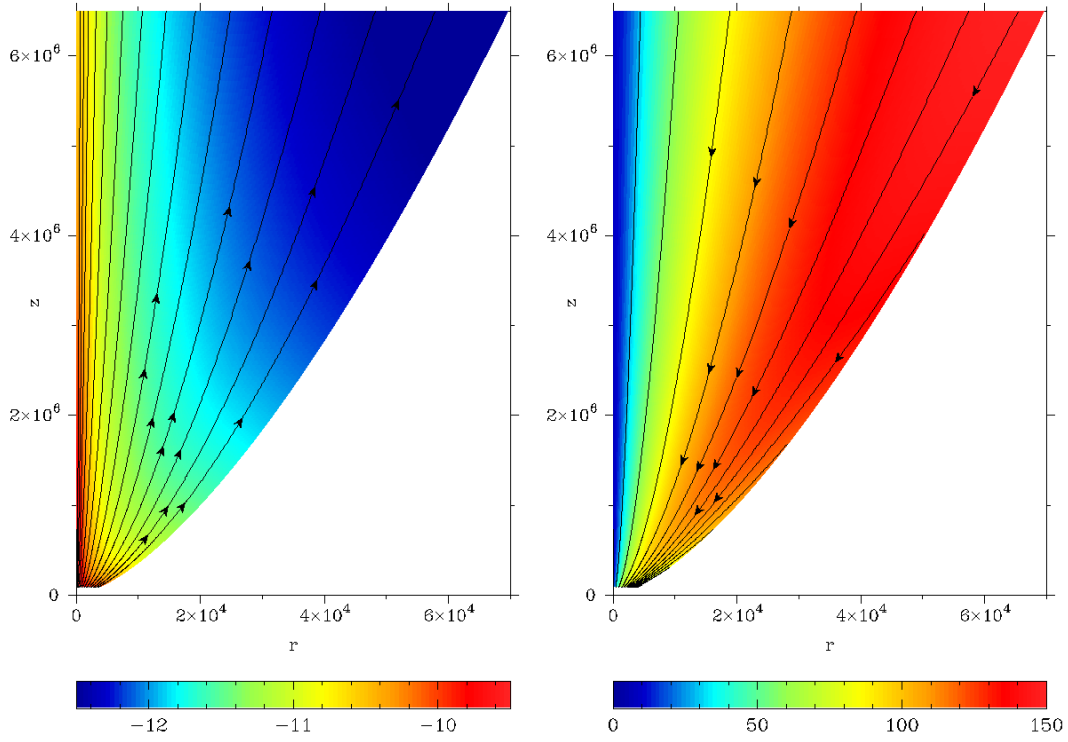


Figure 4. Same as in Fig. 2, but for model B2. The light cylinder radius is $r_{lc} = 1.6$.

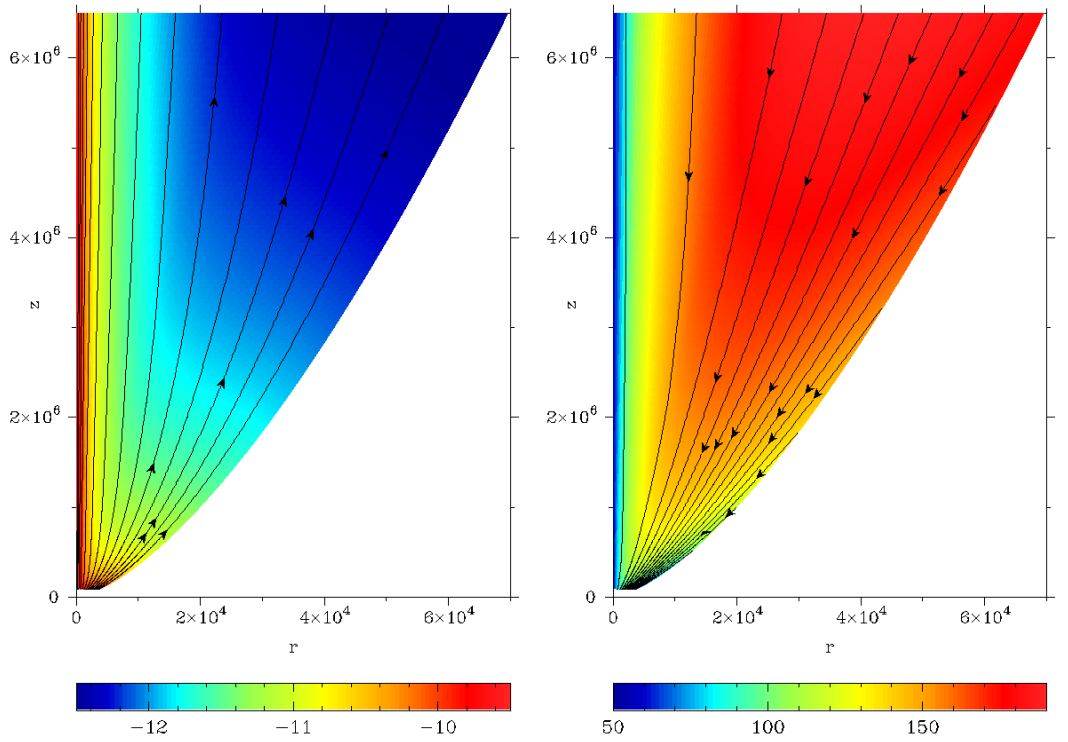


Figure 5. Same as in Fig. 2, but for model B2H. The light cylinder radius is $r_{lc} = 1.6$.

for B^ξ and u^ξ and a zero-gradient condition for all other variables.

3.2 Initial setup

The initial configuration corresponds to a non-rotating, purely poloidal magnetic field with approximately constant magnetic pressure across the funnel. The plasma density within the funnel is set to a small value so that the outflow generated at the inlet boundary can easily sweep it away. In order to speed this process up the η component of velocity inside the funnel is set equal to $0.7c$, whereas the ξ component is set equal to zero.

3.3 Grid extensions

The inner rings of the grid, where the grid cells are small and, therefore, so is also the time step, are the computationally most intensive regions of the simulation domain. If we kept computing these inner rings during the whole run then we would not be able to advance very far from the jet origin. Fortunately, the transonic nature of the jet flow allows us to cease computations in the inner region once the solution there settles to a steady state. To be more precise, we cut the funnel along the ξ -coordinate surfaces into overlapping sectors with the intention of computing only within one sector at any given time, starting with the sector closest to the inlet boundary. Once the solution in the “active” sector settles to a steady state we switch to the subsequent sector, located further away from the inlet. During the switch the solution in the outermost cells of the active sector is copied into the corresponding inner boundary cells of the subsequent sector. During the computation within the latter sector these inner boundary cells are not updated. This procedure is justified only when the flow in a given sector cannot communicate with the flow in the preceding sector through hyperbolic waves, and thus we ensure that the Mach cone of the fast-magnetosonic waves points outward at the sector interfaces (see Paper I).

In these simulations we used up to 7 sectors, with each additional sector being ten times longer than the preceding one. This technique has enabled us to reduce the computation time by more than three orders of magnitude. Although the grid extension can in principle be continued indefinitely, there are other factors that limit how far along the jet one can advance in practice. Firstly, once the paraboloidal jets become highly collimated the required number of grid cells along the jet axis increases, and each successive sector becomes more computationally expensive than the previous one. Secondly, errors due to numerical diffusion gradually accumulate in the downstream region of the flow and the solution becomes progressively less accurate (see Fig. 1).

4 RESULTS

As is generally the case in numerical simulations, our computations are subject to numerical errors, mainly the truncation errors of our RMHD scheme. The field-line constants described in Section 2.1 can be used for a straightforward evaluation of the absolute error. Fig. 1 shows the ideal-MHD constants k , Ω and μ as functions of magnetic flux at the

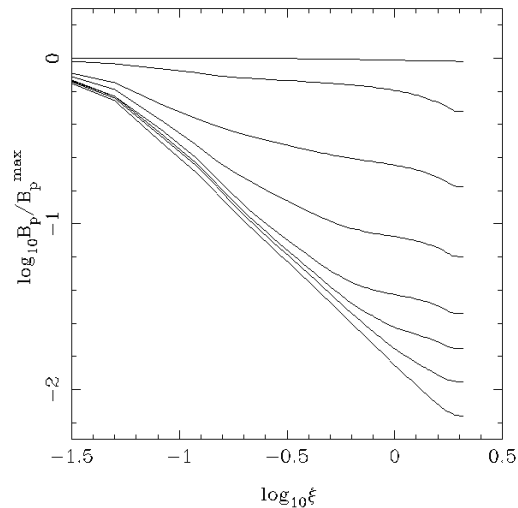


Figure 6. Distribution of the poloidal magnetic field across the jet of model B1, showing the development of an axial core as the distance from the origin increases. From top to bottom, the curves correspond to $\eta = 1, 50, 5 \times 10^2, 5 \times 10^3, 5 \times 10^4, 5 \times 10^5, 5 \times 10^6$ and 5×10^7 , respectively.

inlet and near the outer boundary of the computational domain for models A and B1. If the curves do not exactly coincide, this is indicative of computational errors. Although the plots exhibit noticeable deviations, they remain relatively small, and we conclude that the results are trustworthy.

Figs. 2–5 show the general 2D structure of the derived jet solutions for models A, D, B2 and B2H midway from the inlet surface. We selected these particular cases since they represent the most significant variations in the model parameters, namely the transition (i) from conical to paraboloidal shape of the confining wall (A and B2), (ii) from uniform to differential rotation at the base (A and D)⁴ and (iii) from cold to initially hot flows (B2 and B2H). In general, the structure of the simulated ultra-relativistic jets is very similar to that of the moderately-relativistic conical jets studied in Paper I. All models show the development of a central core where the source-frame mass density $\rho' = \Gamma\rho$ peaks. The mass concentration is accompanied by a bunching-up of the poloidal magnetic field lines near the axis, as further illustrated in Fig. 6. The development of an axial core is a generic property of axisymmetric MHD outflows from a rotating source (Bogovalov 1995) and was also a feature of the jets simulated in Paper I. The distribution of the Lorentz factor across the jet varies, however, from case to case. In model A Γ has its maximum value at the jet boundary (Fig. 2). In model D the maximum is located approximately midway between the symmetry axis and the boundary (Fig. 3). This reflects the fact that the angular velocity of magnetic field lines, and hence the electromagnetic energy flux (equation 20), vanishes at the boundary in this model, resulting

⁴ Note that, when displaying results for model D, we define the fiducial light-cylinder radius in terms of the angular velocity Ω_0 of the innermost field line.

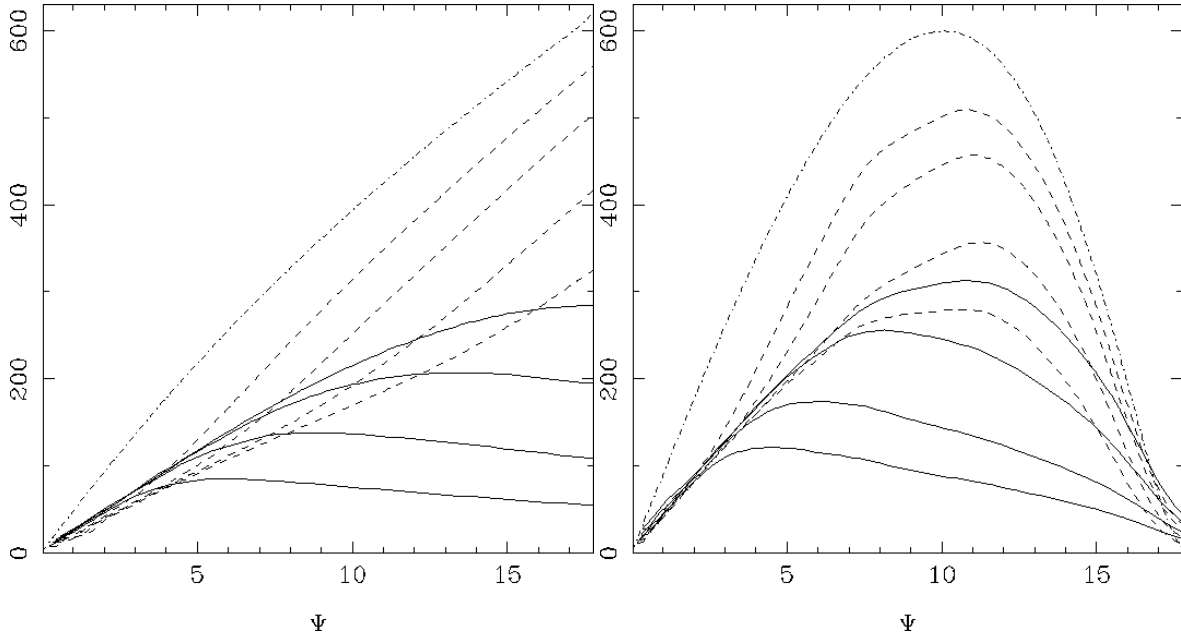


Figure 7. Distribution of Γ and $\mu_m = \mu_h \sigma$ across the jet in models B1 (left panel) and D (right panel). Solid lines show Γ at $\eta = 5 \times 10^4, 5 \times 10^5, 5 \times 10^6, 5 \times 10^7$ (increasing upward), dashed lines show $\mu_h \sigma$ at the same locations (increasing downward), and the dash-dotted line shows μ .

in $\mu \approx \mu_h \approx 1$ near the wall (see Fig. 7). The Lorentz factor of the initially cold jet in model B2 at first peaks near the axis, with its value decreasing slightly on the way to the jet boundary. However, further downstream the maximum shifts towards the boundary and eventually disappears. In the initially hot jet of model B2H the Lorentz factor at first peaks right on the symmetry axis, where the acceleration is due to the gas pressure. However, further downstream its evolution is similar to that of model B2.

Fig. 8 shows the efficiency of plasma acceleration along the magnetic surface $\Psi = 0.8\Psi_{\max}$ (located near the jet boundary) for models B1–B4, which differ only by the strength of the initial magnetization. One can see that in all four cases the kinetic energy flux, $\approx \mu_h \rho u_p c^2 \approx \Gamma \rho u_p c^2$, eventually exceeds the Poynting flux, $\mu_m \rho u_p c^2$. This magnetic surface is not exceptional and a similar behaviour is exhibited along other flux surfaces. This is illustrated by Figs. 7 and 9. These figures also show that soon after reaching equipartition the plasma acceleration slows down significantly: this is consistent with the relation $\mu \approx \Gamma(1 + \sigma)$ obtained from equations (16), (20) and (19), in which crossing the equipartition point corresponds to the magnetization parameter σ dropping below 1. Fig. 8 further indicates that the efficiency of magnetic acceleration is higher the lower the initial magnetization. This is reflected in the behaviour of σ , the ratio of the Poynting flux to the matter energy flux (see Section 2.1). The left panel of Fig. 10 shows that the fast initial decrease of σ slows down at a higher value of σ when the initial magnetization is larger. If this behaviour in fact extends to values of $\mu_{m0} \approx \mu$ that are low enough for the maximum attainable speed to remain nonrelativistic then the indicated inverse correlation is consistent with the very high acceleration efficiency exhibited by MHD outflow solutions in the Newtonian regime (e.g. Vlahakis et al. 2000).

The high efficiency of magnetic acceleration is not unique to models in which the magnetic field lines rotate uniformly. Fig. 7, in which the results for model B1 are compared with those for model D, shows that equally effective acceleration is achievable in the case of a differentially rotating source.

The geometry of the bounding wall has a pronounced effect on the acceleration efficiency, as demonstrated by Fig. 9. A larger value of the power-law index a in the shape function $z \propto r^a$ corresponds to a more rapidly rising function $\Gamma(r/r_{lc})$ along a given magnetic flux surface $\Psi = \text{const}$. Whereas in the model B1 ($a = 3/2$) the acceleration slows down only after the equipartition point, in model A ($a = 1$) this occurs much earlier and, as a result, equipartition between magnetic and kinetic energy is reached only near the jet axis. Equipartition is not reached in model C ($a = 2$) either (see Fig. 9), but for a different reason. Due to the higher degree of external collimation, this jet eventually becomes very thin. This makes our simulation increasingly expensive and we are forced to terminate it before reaching sufficiently large jet radii. (Moreover, the computational errors are accumulated over a longer path along the jet and would become rather high if we continued.) However, Fig. 9 shows that in this model the Lorentz factor is a faster growing function of cylindrical radius compared to model B1. Finally, in model E ($a = 2/3$) we consider a jet propagating in a channel with a progressively diverging wall, which in practice may correspond to the polar funnel of a thick accretion disc (e.g. Paczyński & Wiita 1980). In this case the jet eventually becomes detached from the wall and then expands as a conical outflow (Fig. 11). The acceleration rate is similar to that of model A (see Fig. 12).

The initially hot jet, model B2H, is subject to both magnetic and thermal acceleration, so, as expected, the Lorentz factor in this case grows faster compared to the correspond-

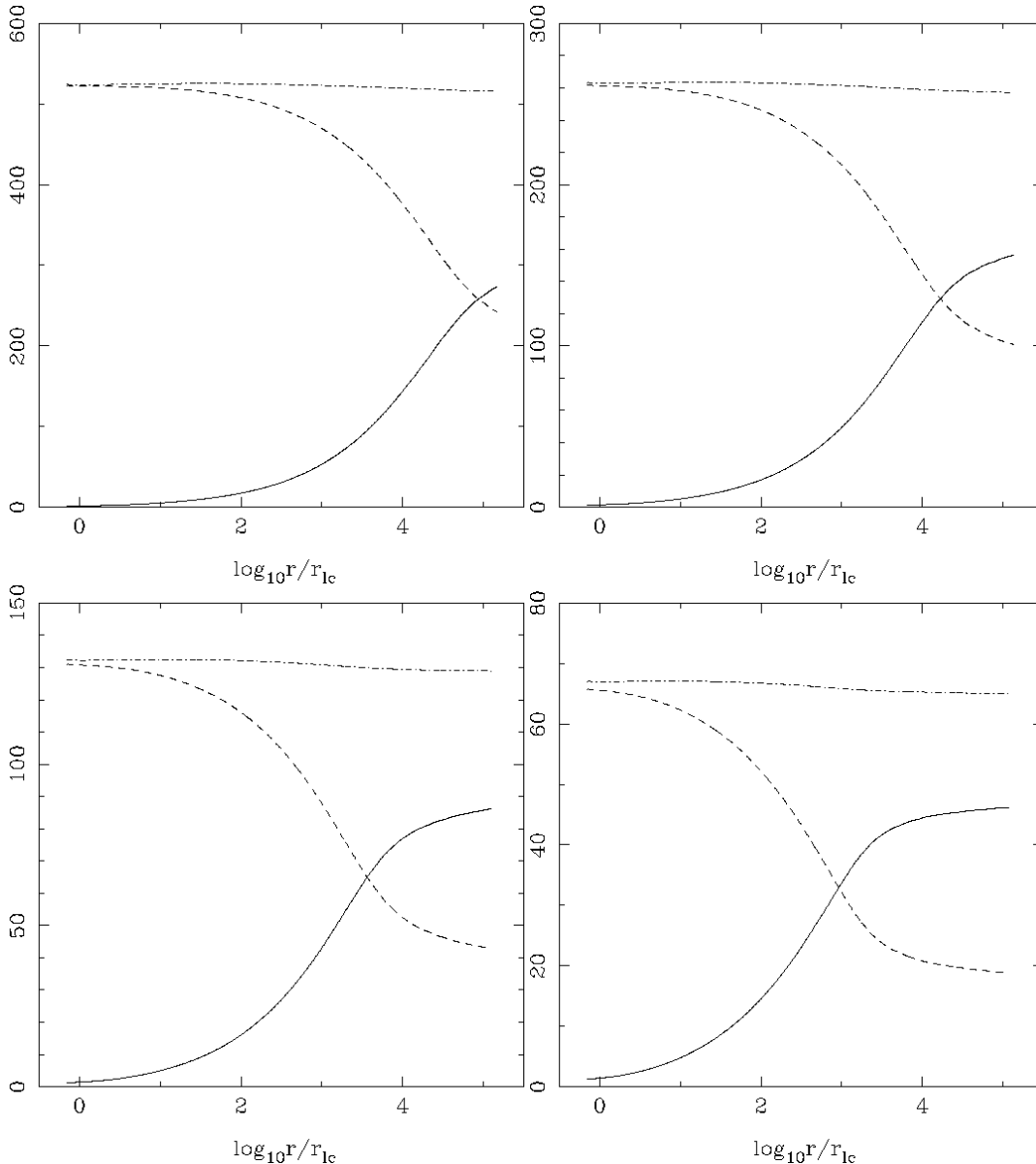


Figure 8. Γ (solid line), $\mu_m = \mu_h \sigma$ (dashed line) and μ (dash-dotted line) along the magnetic field line with $\Psi = 0.8\Psi_{\max}$ as a function of cylindrical radius for models B1 (top left panel), B2 (top right panel), B3 (bottom left panel) and B4 (bottom right panel).

ing cold jet (see the right panel of Fig. 13). But a closer inspection reveals that the acceleration process exhibits a new mode of behaviour in this case (one that was, however, found before in semi-analytic self-similar solutions; see Vlahakis & Königl 2003b). It is seen that a significant fraction of thermal energy is at first converted into Poynting flux. The middle panel of Fig. 13 shows that the Poynting-to-mass flux ratio $\mu_m c^2$ grows until $r \simeq 10^2 r_{1c}$ and only then starts to decline. However, this decrease is quite fast and the terminal value of μ_m for the chosen magnetic flux surface ($\Psi = 0.5\Psi_{\max}$) is, in fact, lower than in the corresponding cold jet (model B2) shown in the left panel of this figure, with a correspondingly higher asymptotic Lorentz factor.

The distribution of the terminal bulk Lorentz factor across these two jet models is shown in right panel of Fig. 13. One can see that on the axis the Lorentz factor of the hot

jet is higher than that of the cold jet by approximately the value of the initial thermal Lorentz factor, $\Gamma_{t0} = 55$. This is as expected given that magnetic acceleration does not operate along the axis. However, at the wall the difference is only half as large and in the middle of the jet it is higher than 40. These traits are evidently a consequence of the thermal-to-Poynting energy conversion and its effect on the poloidal magnetic field distribution, as discussed in Section 5.5.

Although the case of an unconfined wind may not be directly relevant to GRB flows, which are inferred to undergo a fairly efficient collimation (see Section 1), it is certainly of interest to the pulsar community. Furthermore, it is worth investigating from a purely theoretical point of view. The acceleration details for this case (model AW) are presented in Fig. 14. The lower efficiency of magnetic acceleration noted in the conical-wall case (model A), particularly near the jet

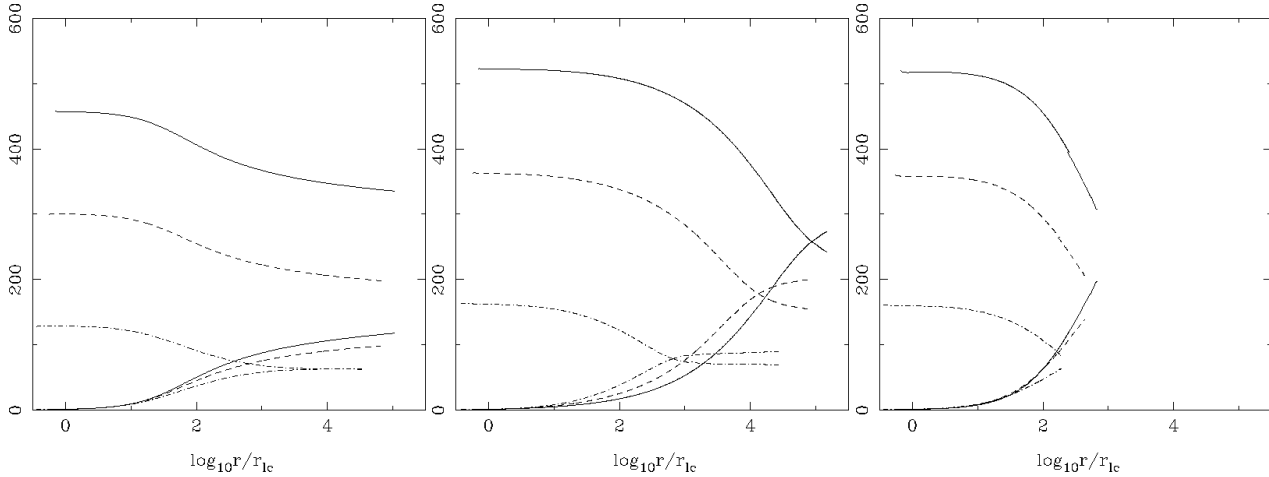


Figure 9. Γ (increasing functions of r) and $\mu_m = \mu_h \sigma$ (decreasing functions of r) along the magnetic field lines $\Psi = 0.8\Psi_{\max}$ (solid lines), $\Psi = 0.5\Psi_{\max}$ (dashed lines) and $\Psi = 0.2\Psi_{\max}$ (dash-dotted lines) in models A (left panel), B1 (middle panel) and C (right panel).

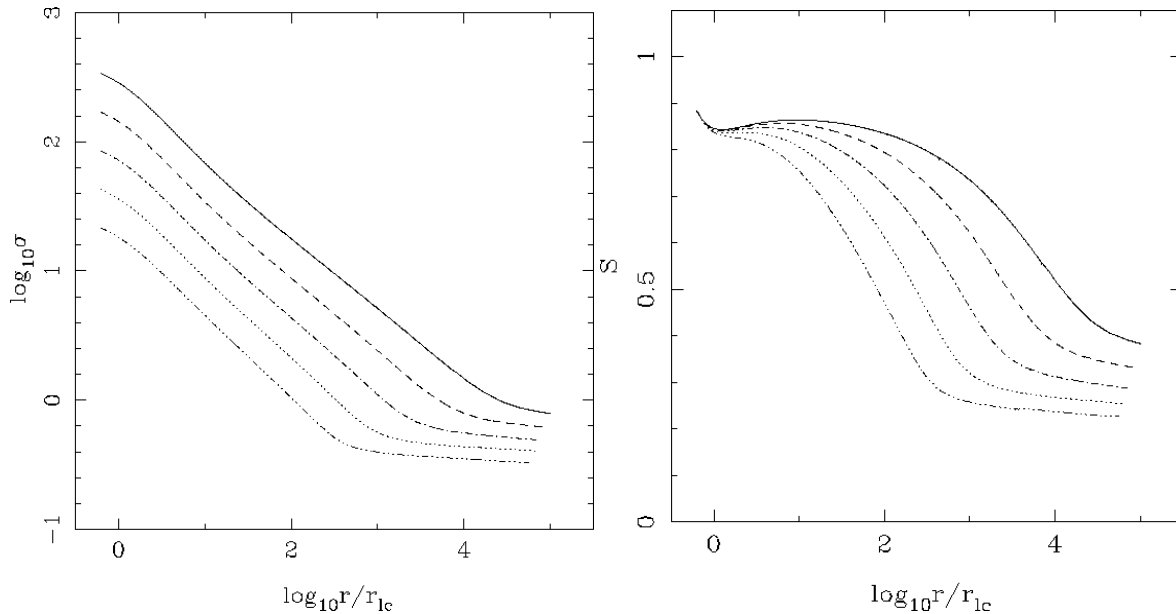


Figure 10. Left panel: Evolution of σ along the magnetic field line $\Psi = 0.8\Psi_{\max}$ in models B1 (solid line), B2 (dashed line), B3 (dash-dotted line), B4 (dotted line) and B5 (dash-triple-dotted line). Right panel: Evolution of the bunching function $S = \pi B_p r^2 / \Psi$ for the same models along the same magnetic field line.

boundary, is even more pronounced in this instance. As can be seen in the right panel of Fig. 14, only $\simeq 5\%$ of the Poynting flux injected at $\simeq 12^\circ$ to the equatorial direction has been converted into kinetic energy by the time the cylindrical radius grew to $r = 10^6 r_{lc}$. Although, as shown in the left panel of Fig. 14, the efficiency is higher near the symmetry axis, the terminal Lorentz factor there remains comparatively low because of the reduced effectiveness of magnetic acceleration as the polar angle approaches zero.

5 ANALYSIS OF THE RESULTS

5.1 Efficiency of magnetic acceleration

The steady-state structure of a magnetized relativistic outflow can be understood by analysing the momentum equation. After the partial integration described in Section 2.1, two more equations remain to be considered, corresponding to the two components of the momentum equation in the poloidal plane. Since the main part of the acceleration occurs in the super-Alfvénic region of the flow, it is sufficient to examine only this regime. We further simplify the discussion by taking the flow to be cold. Thermal effects, when present, in any case only affect the initial acceleration region of the flow; we consider them in Section 5.5. We now proceed to extend the discussion in Paper I by taking the $\Gamma \gg 1$ of

the constituent equations, appropriate for the ultrarelativistic flows simulated in the present work, which enables us to derive analytic scalings.

For cold flows $\mu_h \approx \Gamma$ (equation 19), and from equation (16) one finds that $\Gamma \approx \mu - \mu_m$. Substituting the electric current from equation (24) into equation (20), we get

$$\mu_m \approx \frac{\Psi \Omega^2}{4\pi^2 k c^3} \mathcal{S}, \quad (28)$$

where

$$\mathcal{S} = \frac{\pi r^2 B_p}{\int \mathbf{B}_p \cdot d\mathbf{S}} = \frac{\pi r^2 B_p}{\Psi} = \frac{r |\nabla \Psi|}{2\Psi}. \quad (29)$$

Thus, the flow Lorentz factor can be written as

$$\Gamma \approx \mu - \frac{\Psi \Omega^2}{4\pi^2 k c^3} \mathcal{S}. \quad (30)$$

All the quantities except for \mathcal{S} on the right-hand side of this equation are field-line constants, so an increase in Γ along a field line necessarily requires \mathcal{S} to decrease. The function \mathcal{S} is a measure of how bunched the poloidal field lines are — indeed, it is equal to the ratio of B_p at some cylindrical radius r along the field line to the mean magnetic field within that radius, $\Psi/\pi r^2$. For example, for a flow confined within a sufficiently small angle that satisfies $B_p \propto r^\lambda$, $\Psi \propto r^{\lambda+2}$ and

$$\mathcal{S} = \frac{\lambda + 2}{2}.$$

For a uniform distribution of B_p this yields $\mathcal{S} = 1$, whereas one has $\mathcal{S} > 1$ if B_p increases with r and $\mathcal{S} < 1$ if it decreases. This shows that magnetic acceleration requires a gradual concentration of magnetic flux in the central part of the flow. In the case of a collimating flow this can be achieved through a faster collimation of the inner magnetic flux surfaces than of the outer ones, and in the case of a decollimating flow a faster decollimation of the outer flux surfaces is required. Fig. 6 illustrates the concentration of magnetic flux toward the axis in one of our simulations. In this case, at large distances the poloidal magnetic field scales roughly as $B_p \propto r^{-1.2}$, corresponding to $\mathcal{S}_\infty \sim 0.4$. This is indeed the asymptotic value of \mathcal{S} , as shown in Fig. 15.

Equation (30) is a consequence of the momentum equation along the flow. It shows how Γ increases by the action of the $(1/c)\mathbf{J}_p \times \mathbf{B}_\phi$ force when the function \mathcal{S} decreases along the flow, thereby demonstrating the intimate connection between the acceleration efficiency and the evolution of the poloidal shape of the flow. In evaluating this efficiency we can use \mathcal{S}_f , the value of \mathcal{S} at the fast surface, as a convenient proxy for the initial value of \mathcal{S} . This is because, for $\mu \gg 1$, Γ remains $\ll \mu$ on this surface (e.g. Komissarov 2004). In this case the two terms on the right-hand side of equation (30) are comparable, and we obtain

$$\mathcal{S}_f = \frac{4\pi^2 k \mu c^3}{\Psi \Omega^2}.$$

We can legitimately use equation (30) since the fast surface lies well outside the light cylinder and hence is in the super-Alfvénic domain for most of the simulated field lines. We now utilize this equation to write the asymptotic Lorentz factor in the form

$$\Gamma_\infty \approx \mu(1 - \mathcal{S}_\infty/\mathcal{S}_f). \quad (31)$$

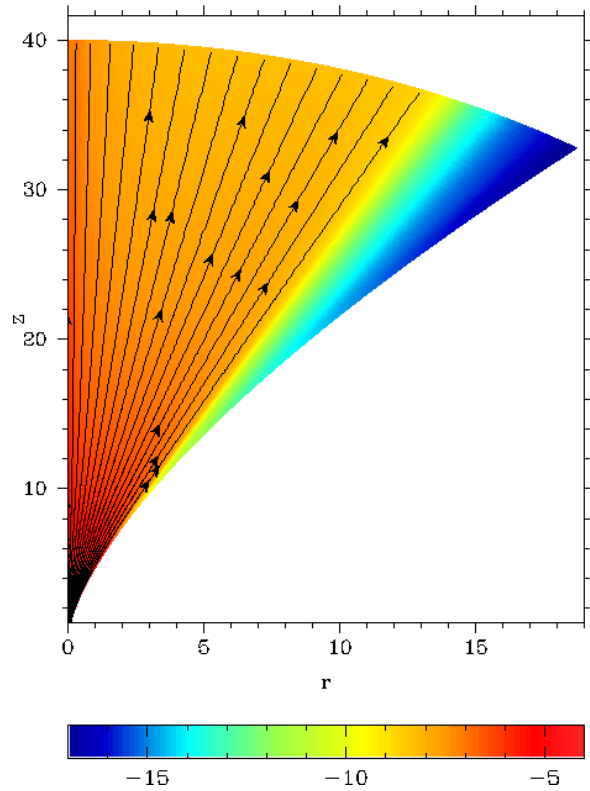


Figure 11. Colour image shows $\log_{10} p_{\text{tot}}$ (with the total pressure given by $p_{\text{tot}} = p + B_{\text{co}}^2/8\pi$, where B_{co} is the comoving magnetic field) and the contours show the magnetic field lines for model E. In this model the light cylinder radius is $r_{\text{lc}} = 0.29$.

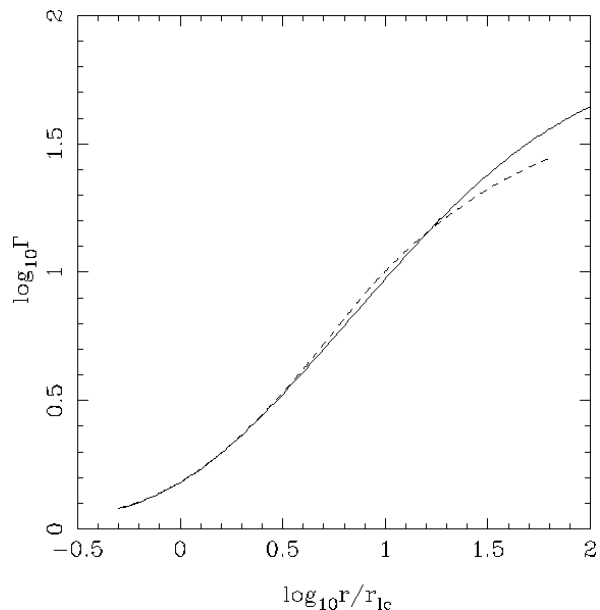


Figure 12. Lorentz factor along the magnetic field line with $\Psi = 0.5\Psi_{\text{max}}$ for model A (solid line) and model E (dashed line).

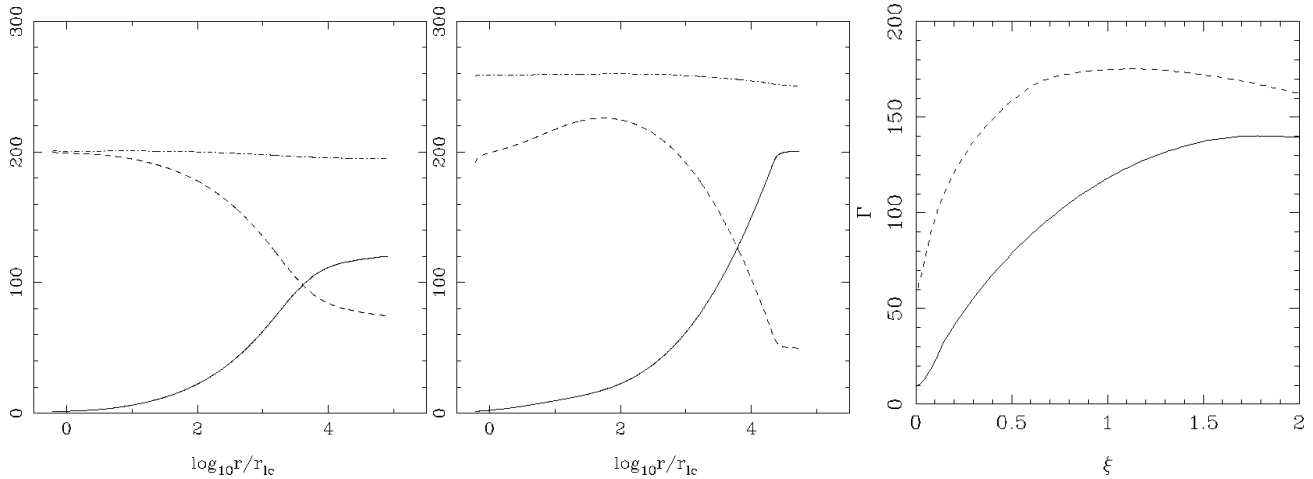


Figure 13. Effects of thermal acceleration. Left panel: cold jet of model B2. Middle panel: hot jet of model B2H (with $w_0/\rho_0 c^2 = 55$). The lines show Γ (solid line), μ (dash-dotted line), $\mu_m = \mu_h \sigma$ (dashed line) and $(w/\rho c^2 - 1)\Gamma$ (dotted line) along the magnetic field line with $\Psi = 0.5\Psi_{\max}$ as a function of cylindrical radius. Right panel: Lorentz factor across the jet at $\eta = 4 \times 10^6 r_{1c}$ for the cold jet of model B2 (solid line) and the hot jet of model B2H (dashed line).

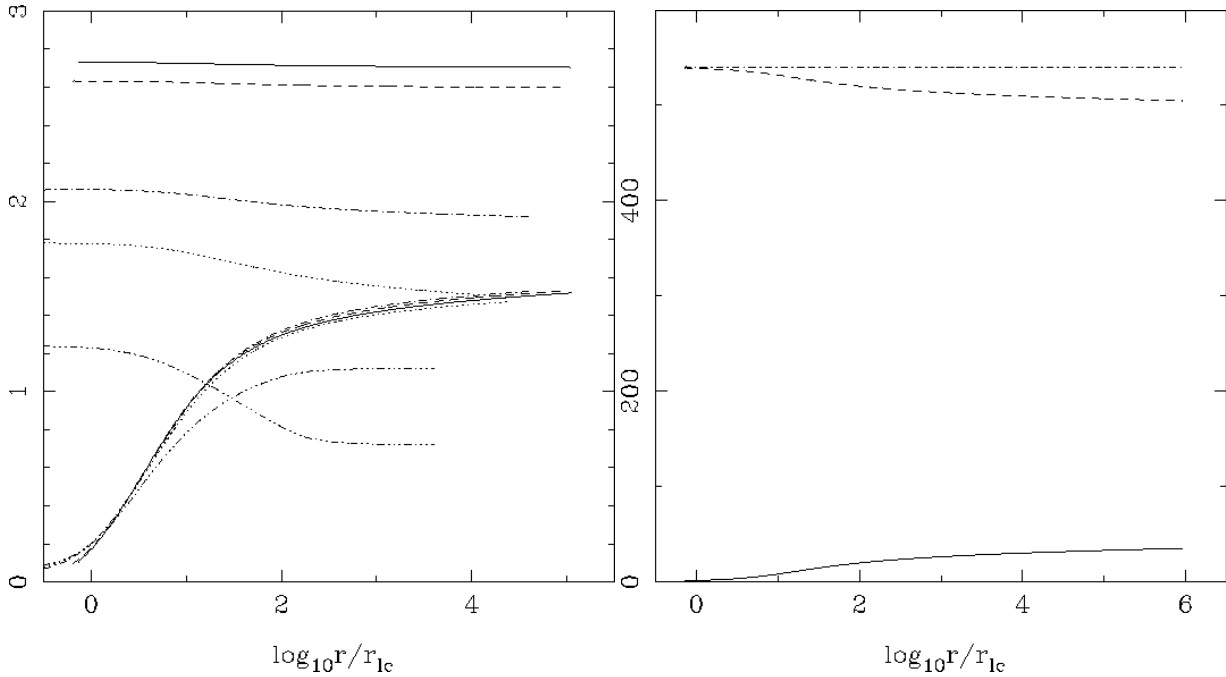


Figure 14. Unconfined wind solution (model AW). Left panel: Lorentz factor (increasing function) and $\mu_h \sigma$ (decreasing function) along five different magnetic field lines: $\Psi = 0.8\Psi_{\max}$ (solid line), $\Psi = 0.5\Psi_{\max}$ (dashed line), $\Psi = 0.2\Psi_{\max}$ (dash-dotted line), $\Psi = 0.1\Psi_{\max}$ (dotted line), $\Psi = 0.027\Psi_{\max}$ (dash-triple-dotted line), the last line originating from the same point at the inlet as the $\Psi = 0.8\Psi_{\max}$ line of model A. Right panel: Γ (solid line), $\mu_h \sigma$ (dashed line) and μ (dash-dotted line) along the magnetic field line with $\Psi = 0.8\Psi_{\max}$ as a function of cylindrical radius.

In our simulations $\mathcal{S}_f \approx 0.9$ (see Figs. 10 and 15). This value reflects the adopted uniform distribution of $B^{\hat{\eta}}$ at the inlet.⁵ Beyond the Alfvén surface the azimuthal magnetic field component becomes dominant, and its hoop stress causes

the inner flux surfaces to collimate faster than the outer ones. As a result \mathcal{S} decreases, attaining asymptotic values $\mathcal{S}_{\infty} \approx 0.25 - 0.4$ for paraboloidal jets (see Figs. 10 and 15). The implied asymptotic Lorentz factors thus satisfy

$$\Gamma_{\infty}/\mu \approx 0.55 - 0.72,$$

⁵ As we already in Section 3.1.1, we have experimented with other distributions that put more flux near the axis and observed a quick “uniformization” of magnetic flux in the immediate vicinity of the inlet under the action of magnetic pressure.

which are indeed the values reached by our simulated flows (see Figs. 7–9). This result indicates that $\gtrsim 50\%$ of the initial Poynting flux is converted into kinetic energy of bulk motion (see also Vlahakis 2004b). The significantly lower efficiency

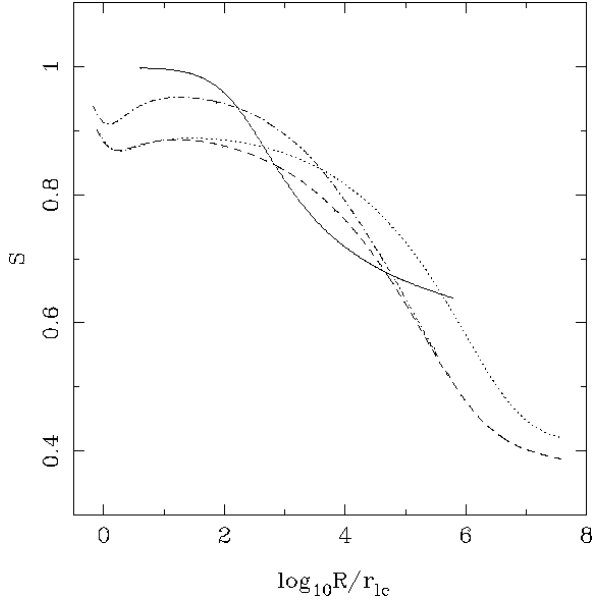


Figure 15. Evolution of the function $\mathcal{S} = \pi B_p r^2 / \Psi$ along the magnetic field line with $\Psi = 0.5\Psi_{\max}$ in models A (solid line), B1 (dashed line), C (dash-dotted line) and D (dotted line).

found in our simulations of flows inside conical and diverging funnels, down to 25% near the boundary (models A and E), is most likely due to the loss of causal connection across the flow (see Section 5.4).

5.2 Power-law acceleration phase

Next we analyse the trans-field component of the momentum equation. The asymptotic form of the trans-field equation in the highly relativistic limit is

$$\frac{\Gamma^2 r}{\mathcal{R}} \approx \frac{\left(\frac{2I}{\Omega B_p r^2}\right)^2 r \nabla \ln \left| \frac{I}{\Gamma} \right| \cdot \frac{\nabla \Psi}{|\nabla \Psi|}}{1 + \frac{w}{\rho c^2} \frac{4\pi \rho u_p^2 r_{\text{lc}}^2}{B_p^2 r^2}} - \Gamma^2 \frac{r_{\text{lc}}^2}{r^2} \frac{\nabla r \cdot \nabla \Psi}{|\nabla \Psi|} \quad (32)$$

where \mathcal{R} is the curvature radius of poloidal field lines (see equation 16 and related discussion in Vlahakis 2004a). The three terms of this equation are the poloidal curvature term (left-hand side), the electromagnetic term (first on the right-hand side), which is of order 1, and the centrifugal term (second on the right-hand side). This important equation, with the centrifugal term omitted, was derived by Chiueh et al. (1991), Lyubarsky & Eichler (2001), and Okamoto (2002), while Bogovalov (1995), Beskin & Malyskin (2000), and Tomimatsu & Takahashi (2003) derived the same equation with the centrifugal term included but the poloidal curvature term omitted.

Well outside the light cylinder, where $r\Omega \gg v^{\hat{\phi}}$ and $v \simeq c$, equations (26) and (27) imply

$$r B^{\hat{\phi}} = -\frac{1}{c} \Omega B_p r^2. \quad (33)$$

From this equation and equation (18) one finds that

$$I = -\frac{1}{2} \Omega B_p r^2, \quad (34)$$

where B_p is the magnitude of the poloidal magnetic field. Substituting this result into equation (20) one also finds that

$$\mu_m = \frac{1}{4\pi} \frac{r^2}{r_{\text{lc}}^2} \frac{B_p^2 \Gamma}{\rho u_p^2}. \quad (35)$$

Thus, in this regime one can rewrite equation (32) as

$$\frac{\Gamma^2 r}{\mathcal{R}} \approx \frac{r \nabla \ln \left| \frac{I}{\Gamma} \right| \cdot \frac{\nabla \Psi}{|\nabla \Psi|}}{1 + \frac{\mu_h}{\mu_m}} - \Gamma^2 \frac{r_{\text{lc}}^2}{r^2} \frac{\nabla r \cdot \nabla \Psi}{|\nabla \Psi|}. \quad (36)$$

In the magnetically dominated case, where $\mu_m \gg \mu_h$, order-of-magnitude evaluation of the last two terms in this equation gives the useful result

$$\frac{\Gamma^2 r}{\mathcal{R}} \approx 1 - \Gamma^2 \frac{r_{\text{lc}}^2}{r^2}. \quad (37)$$

Depending on which term in equation (32) can be neglected, we can isolate the following three cases (ordered by increasing importance):

(i) If the electromagnetic part is negligible then the shape of the flow is determined by the centrifugal term, resulting in a hyperbolic line shape, a characteristic of ballistic motion (see equation 20 and related discussion in Vlahakis 2004a; see also Sections 5.3.1 and A1.3). None of the end-states of our simulations has this property.

(ii) If the poloidal curvature term is negligible, the electromagnetic and centrifugal terms balance each other. This is the case very close to the rotation axis (inside the cylindrical core) as well as for a quasi-conical flow like our model A and for paraboloidal flows with $a > 2$ as in our model F (see Section 5.3). In this case equation (37) gives

$$\Gamma \simeq \frac{r}{r_{\text{lc}}}. \quad (38)$$

Following different methods, this ‘‘linear acceleration case’’ was found by Contopoulos & Kazanas (2002), who analysed radial force-free flows beyond the light cylinder (and hence their analysis holds in the regime between the Alfvén and the fast-magnetosonic surfaces), and by Beskin et al. (1998), who perturbed a quasi-conical flow (and found that $\Gamma \approx r/r_{\text{lc}}$ applies in the sub-fast-magnetosonic regime). Our results for models A and F agree with the scaling $\Gamma \approx r/r_{\text{lc}}$; see the top left panel of Fig. 17.

(iii) If the centrifugal term is negligible then the shape of the flow is determined by the electromagnetic force. This regime applies to the case of paraboloidal wall with $a \leq 2$ (see Section 5.3). Equation (37) implies that in this case the radius of curvature of poloidal field lines is

$$\mathcal{R} \approx \Gamma^2 r. \quad (39)$$

Now, consider a field line of the shape, $z \propto r^b$. (In what follows we use the superscript b to indicate the power-law index that describes the shape of given magnetic field lines, whereas the superscript a is reserved for the power-law index that gives the shape of the funnel wall in our numerical models. Note that the interior field lines in these models have b that is slightly larger than a , although $b \rightarrow a$ as the wall is approached; see Fig. 16.) The curvature radius of such a line satisfies

$$\frac{r}{\mathcal{R}} = -r \left(\frac{B_z}{B_p} \right)^3 \frac{\partial^2 r}{\partial z^2} \approx \frac{b-1}{b^2} \left(\frac{r}{z} \right)^2, \quad (40)$$

where the final form is valid when $B_p \approx B_z$. Combining this with equation (39) we get

$$\Gamma \sim \frac{b}{\sqrt{b-1}} \frac{z}{r} \propto r^{b-1} \propto z^{(b-1)/b} \quad (41)$$

(see also Vlahakis & Königl 2003b), which applies when the power-law index lies in the range $1 < b \leq 2$ and shows that the spatial growth of the Lorentz factor is also a power law in this case (in either r or z). Assuming that the flow is not too collimated within the light cylinder, so that $z_{lc} \simeq r_{lc}$ for most of the field lines (an assumption that is well satisfied in our numerical models), we can write the above result in the following useful forms:

$$\Gamma \simeq (r/r_{lc})^{b-1} \quad \text{or} \quad \Gamma \simeq (R/r_{lc})^{(b-1)/b}. \quad (42)$$

This acceleration regime operates in our $1 < a \leq 2$ numerical models before the flow reaches approximate equipartition, as can be verified by inspecting Figs. 17 and 18.

The direct dependence of the flow acceleration on the poloidal curvature of the magnetic field lines in the regime (iii) leads to an anti-correlation between the jet Lorentz factor and its opening angle. For a line shape $z \propto r^b$ ($1 < b \leq 2$) we find

$$\Gamma \tan \theta_v = 1/\sqrt{b-1}, \quad (43)$$

where $\theta_v \equiv \arctan(dr/dz)$ is the local half-opening angle of the magnetic flux surface. Fig. 19 shows the variation of $\Gamma \tan \theta_v$ along the flux surface $\Psi = 0.8\Psi_{\max}$ of model B1. One can see that this product is indeed close to $1/\sqrt{b-1}$. It is, however, not exactly a constant, for the following reasons: the curvature acceleration regime is not really applicable at small and large spherical radii, the electromagnetic term in equation (32) is not exactly equal to 1, and the power-law index b varies along the flow. The figure nevertheless indicates that equation (43) provides a useful estimate of the relationship between Γ and θ_v .

As expected from our discussion in Section 5.1 of the close connection between the acceleration efficiency and the evolution of the poloidal field-line shape, the trans-field force balance equation, which determines the variation of the flux-surface shape along the flow, is seen to provide information on how fast the Lorentz factor increases with distance from the source. For all shape functions $z \propto r^b$ with $1 < b \leq 2$, the corresponding power-law dependence of Γ leads to a high ($\gtrsim 50\%$) magnetic-to-kinetic energy conversion efficiency over astrophysically relevant distances. Using equation (42) we find that equipartition between the Poynting and kinetic energy fluxes is attained at a cylindrical radius

$$r_{\text{eq}} = r_0 \left(\frac{\mu}{2\Gamma_0} \right)^{1/(b-1)}. \quad (44)$$

After substitution $r_0 = r_{lc}$ and $\Gamma_0 = 1$, this equation reads

$$r_{\text{eq}} = r_{lc} \left(\frac{\mu}{2} \right)^{1/(b-1)}, \quad (45)$$

which, in fact, agrees very well with our results for models B (see Fig. 19). In terms of the spherical radius, assuming again that $R_{lc} \simeq r_{lc}$, we can write this expression as

$$R_{\text{eq}} = r_{lc} \left(\frac{\mu}{2} \right)^{b/(b-1)}. \quad (46)$$

For $b > 2$ the corresponding relations are (using equation 38) $r_{\text{eq}} = (\mu/2)r_{lc}$ and $R_{\text{eq}} = (\mu/2)^b r_{lc}$.

The derived scaling for the Lorentz factor can be used to find the behaviour of other quantities. For example, for the main part of the flow in which the Poynting flux dominates the energy flux, one has $\sigma\Gamma \approx \mu$ and hence, for $1 < b \leq 2$,

$$\sigma \approx \mu/\Gamma \propto r/z \propto r^{-(b-1)}. \quad (47)$$

The predicted behaviour is indeed seen in the left panel of Fig. 10. This figure further shows that the ‘‘self similar’’ structure of the magnetization curves extends also beyond the equipartition radius, where they flatten out; in particular, they do not cross each other even in that regime. Consequently, the magnetization beyond the turning point of the curve is lower the smaller the inlet value, which goes along with our finding that the efficiency $\sim 1/(1 + \sigma_\infty)$ of magnetic-to-kinetic energy conversion in cold flows decreases with increasing initial magnetization.

The high acceleration efficiencies attained by our simulated flows appear to be inconsistent with the conclusion of Chiueh et al. (1998) that a transition to a low- σ configuration cannot occur gradually in regions well beyond the light cylinder, where the flow has become ultra-relativistic. Their analysis was, however, based in part on an estimate of the change in the angle θ_v between the poloidal flow and the rotation axis as one moves through a length $\Delta\ell$ along the flow (see text after equation 14 in their paper): this estimate is not generally valid since it assumes that $\Delta\ell \sim \Delta r$, which only applies to quasi-radial flows. If instead we use $\Delta\ell \sim \Delta z$ in equation (14) of Chiueh et al. (1998) and concentrate on paraboloidal flows ($z \propto r^b$) with $b \leq 2$, we get $\Delta\theta_v \sim \Delta(z/r)b/\Gamma^2(b-1)$, which yields the scaling $\Gamma \propto z/r$ found above. On the other hand, the lower acceleration efficiency exhibited by our model A, in which the flow morphology is quasi-radial (see Figs. 2, 9 and 15), appears to be consistent with the Chiueh et al. (1998) inference of logarithmic collimation and slower acceleration. We note in this connection that, beyond the end of the power-law acceleration phase analysed in this subsection, it is possible to have an additional, logarithmic acceleration regime in which potentially up to 100% of the Poynting flux could be converted into matter kinetic energy flux (see Vlahakis 2004a and references therein). However, this acceleration is too slow to be of astrophysical interest since it requires exponentially large distances for completion.

5.3 Dependence on the external pressure distribution

Although we have chosen, for numerical convenience, to prescribe the shape of the funnels that guide our simulated flows, in reality the boundary shape of pressure-confined flows will be determined by the ambient pressure distribution, p_{ext} , and we expect a one-to-one correspondence between the shape of the boundary and the parameters of the confining medium, enforced through the pressure-balance condition at the boundary, $p_{\text{int}} = p_{\text{ext}}$. Here we analyse this issue for the asymptotic region of a magnetically accelerated flow, where the internal jet pressure, p_{int} , is dominated by the contribution due to the azimuthal component of mag-

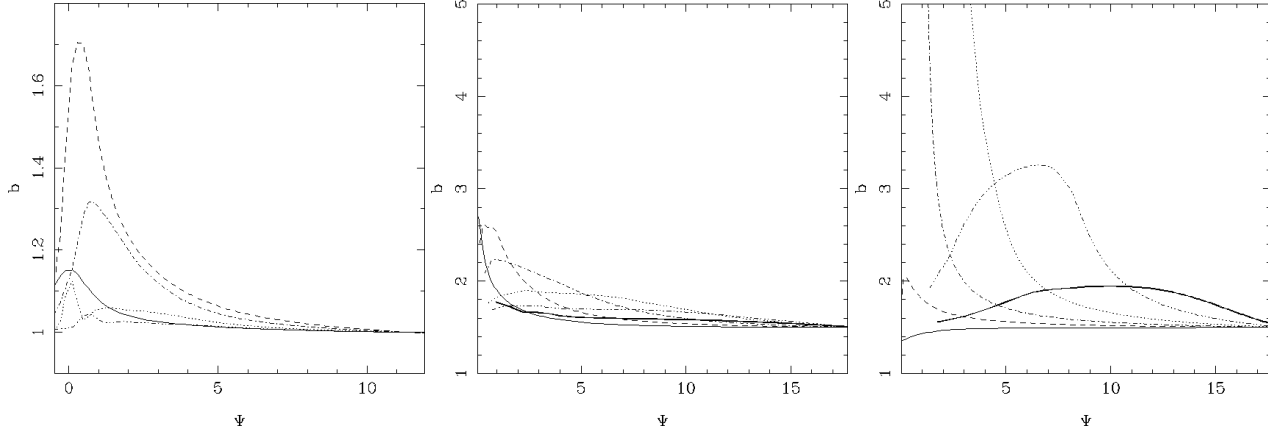


Figure 16. The exponent b of the poloidal shape function $z \propto r^b$ for models A (left panel), B2 (middle panel) and B2H (right panel) across the jet. For model A the depicted cross sections are at $R = 10$ (solid line), $R = 10^2$ (dashed line), $R = 10^3$ (dash-dotted line), $R = 10^4$ (dotted line) and $R = 10^5$ (dash-triple-dotted line). For models B2 and B2H the plotted cross sections are at $\eta = 5 \times 10^2$ (thin solid line), $\eta = 5 \times 10^3$ (dashed line), $\eta = 5 \times 10^4$ (dash-dotted line), $\eta = 5 \times 10^5$ (dotted line), $\eta = 5 \times 10^6$ (dash-triple-dotted line) and $\eta = 5 \times 10^7$ (thick solid line).

netic field, $p_{\text{int}} = p + B_{\text{co}}^2/8\pi \simeq (B^{\hat{\phi}})^2/8\pi\Gamma^2$. Thus,

$$\Gamma^{-2} = \frac{8\pi p_{\text{ext}}}{(B^{\hat{\phi}})^2}.$$

In the following we assume that the external pressure distribution is a power-law

$$p_{\text{ext}} = p_{\text{ext,lc}}(z/z_{\text{lc}})^{-\alpha},$$

which is consistent with the funnel shape $z \propto r^a$ adopted in our numerical simulations. Moreover, since $\mu_m \propto I \propto rB^{\hat{\phi}}$ (see equations 18, 20) is a weak function of distance we may assume that at the jet boundary $B^{\hat{\phi}} = B_{\text{lc}}^{\hat{\phi}}(r/r_{\text{lc}})^{-1}$. Then we have

$$\Gamma^{-2} = Cx^2Z^{-\alpha}, \quad (48)$$

where $x \equiv r/r_{\text{lc}}$ and $Z \equiv z/r_{\text{lc}}$ are the dimensionless coordinates of the jet boundary and

$$C = \left(\frac{8\pi p_{\text{ext}}}{B_{\hat{\phi}}^2} \right)_{\text{lc}} \left(\frac{z_{\text{lc}}}{r_{\text{lc}}} \right)^{\alpha} = \frac{(z_{\text{lc}}/r_{\text{lc}})^{\alpha}}{\Gamma_{\text{lc}}^2}. \quad (49)$$

It is easy to see that C is a positive dimensionless constant of the order of 1. Provided that $dr/dz \ll 1$ we can approximate the curvature radius of the jet boundary via

$$\mathcal{R}^{-1} \approx -\frac{d^2r}{dz^2} = -\frac{1}{r_{\text{lc}}} \frac{d^2x}{dZ^2} \quad (50)$$

and rewrite equation (37) as

$$x \frac{d^2x}{dZ^2} + \frac{1}{\Gamma^2} - \frac{1}{x^2} \approx 0. \quad (51)$$

After the substitution of Γ from equation (48) this yields an ordinary differential equation for the jet boundary

$$\frac{d^2x}{dZ^2} + C \frac{x}{Z^{\alpha}} - \frac{1}{x^3} = 0. \quad (52)$$

The first term on the left-hand side of equation (52) represents the effect of poloidal curvature, the second is the electromagnetic term and the third is the centrifugal term.

Equation (52) can be solved in closed form in various limits, as described in Appendix A. Here we simplify the discussion by looking for almost power-law solutions

$$x = K^{-1}Z^{1/a}, \quad (53)$$

with K being positive constants and a varying very slowly. Substituting this ansatz into equation (52) and ignoring all terms including derivatives of a , we obtain

$$\frac{1}{a} \left(\frac{1}{a} - 1 \right) + CZ^{2-\alpha} - K^4 Z^{2-4/a} = 0. \quad (54)$$

We now proceed to analyse this equation for different values of the exponent α .

5.3.1 $\alpha > 2$

In this case the second term on the left-hand side of equation (54) vanishes as $Z \rightarrow \infty$ and the only acceptable asymptotic value of a is unity. Indeed, for $a > 2$ the third term diverges, for $a = 2$ it is constant but negative and so is the first term, for $a < 2$ it vanishes and so must the first one, implying $a \rightarrow 1$. Thus, asymptotically the boundary adopts conical shape.

- When $\alpha < 4$ the electromagnetic term of equation (54) dominates over the centrifugal term, and thus $a \rightarrow 1^+$ (since the first term must be negative in order to cancel the second). The boundary shape is therefore *paraboloidal* (with conical asymptotes). An explicit solution of equation (52) in this limit is given in Appendix A.

- When $\alpha > 4$ the centrifugal term dominates over the electromagnetic term in equation (54) and thus $a \rightarrow 1^-$ (since the first term must be positive in order to cancel the third). This is case (i) of our analysis of equation (36), which corresponds to a *hyperboloidal* shape (with conical asymptotes), as demonstrated in Appendix A through an explicit solution of equation (52) in this limit.

- When $\alpha = 4$ one can obtain a solution that is conical ($a = 1$) from the start, with $K^4 = C$. This solution corresponds to our conical model A during the acceleration phase, when $\Gamma \propto r$ (see equation 38). Fig. 20 verifies the predicted

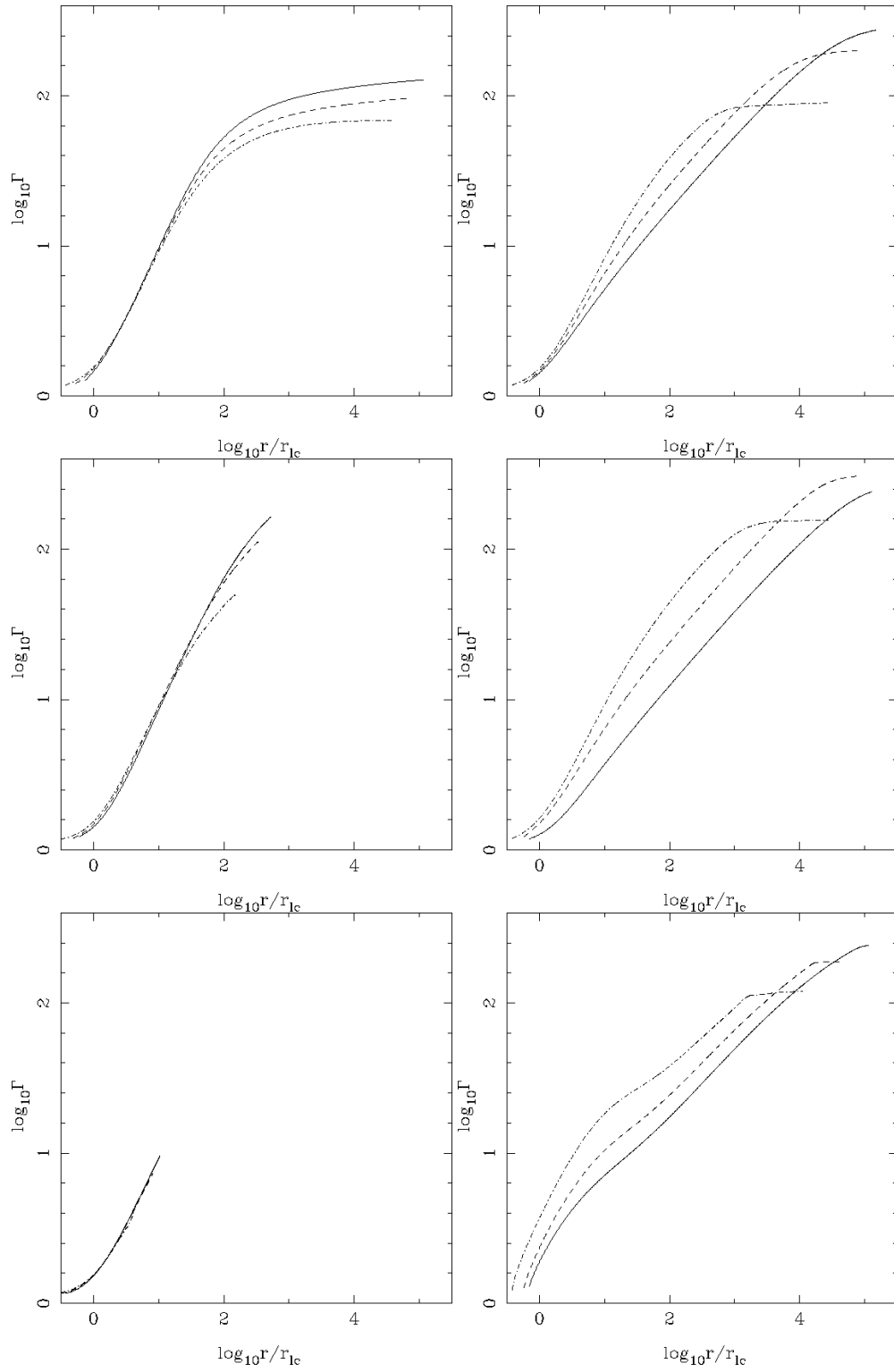


Figure 17. Lorentz factor along three different magnetic field lines of models A (top left panel), B1 (top right panel), C (middle left panel), D (middle right panel), F (bottom left panel), and B2H (bottom right panel) as a function of the cylindrical radius r . Solid line: $\Psi = 0.8\Psi_{\max}$; dashed line: $\Psi = 0.5\Psi_{\max}$; dash-dotted line: $\Psi = 0.2\Psi_{\max}$.

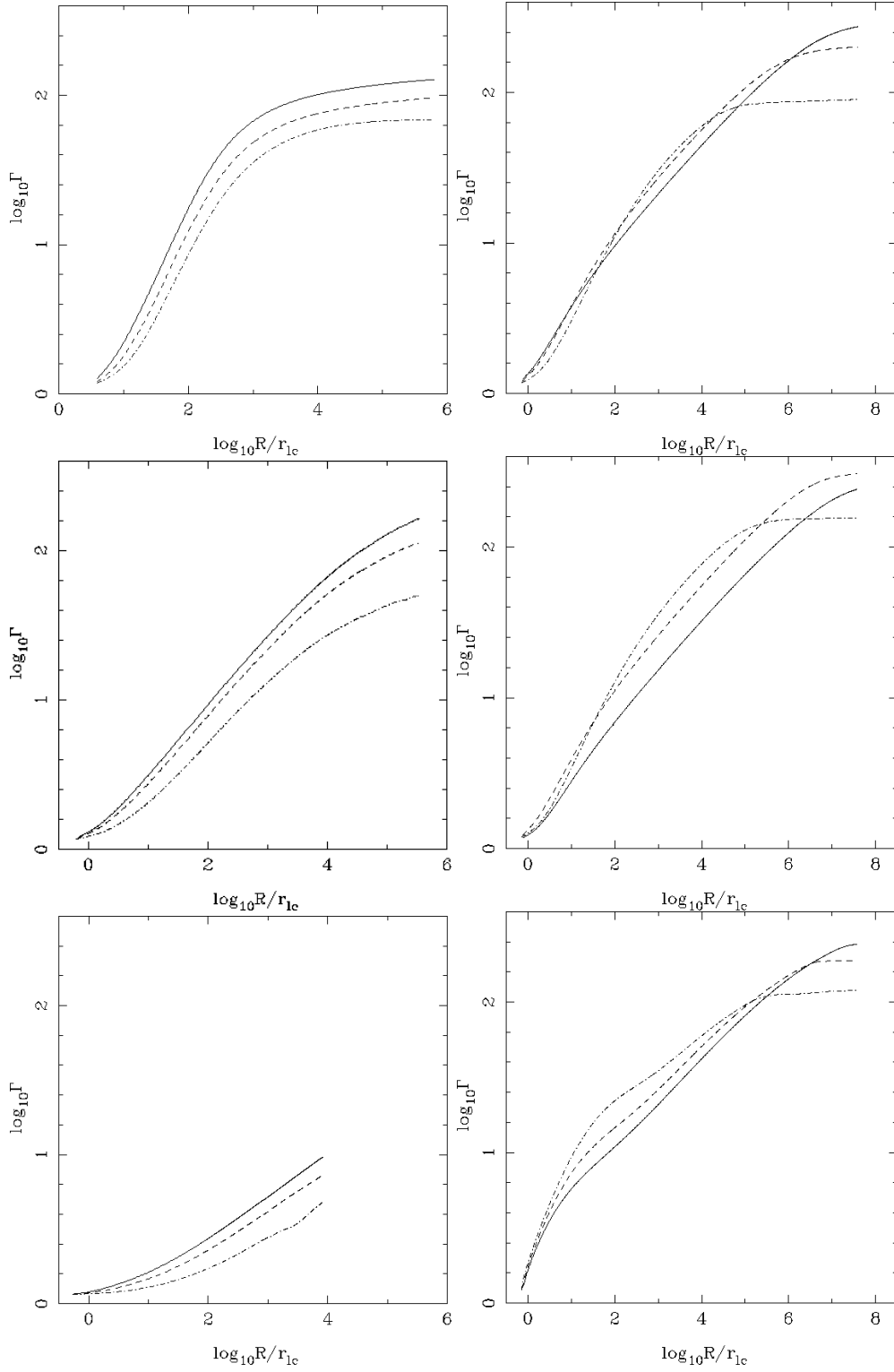


Figure 18. Lorentz factor along three different magnetic field lines of models A (top left panel), B1 (top right panel), C (middle left panel), D (middle right panel), F (bottom left panel), and B2H (bottom right panel) as a function of the spherical radius R . Solid line: $\Psi = 0.8\Psi_{\max}$; dashed line: $\Psi = 0.5\Psi_{\max}$; dash-dotted line: $\Psi = 0.2\Psi_{\max}$.

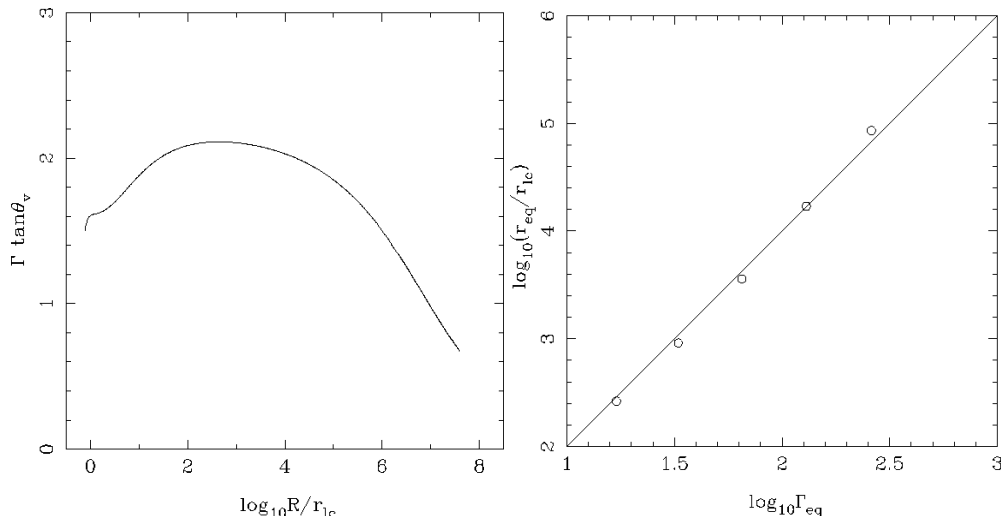


Figure 19. Left panel: variation of $\Gamma \tan \theta_v$ along the flux surface $\Psi = 0.8\Psi_{\max}$ of model B1. Right panel: the diamonds show the equipartition radius (where the Poynting and kinetic energy fluxes are equal) along $\Psi = 0.8\Psi_{\max}$ as a function of the magnetization parameter μ for models B1–B5. The solid line shows the function $\log_{10}(r/r_{1c}) = 2 \log_{10}(\mu/2)$.

scaling ($p_{\text{ext}} \propto Z^{-4}$) and also shows that, after the growth of Γ saturates, a conical shape can be maintained only if the ambient pressure scales as z^{-2} , which follows directly from the scaling $p_{\text{int}} \propto \Gamma^{-2}r^{-2}$ discussed at the beginning of this subsection.

In summary, for $\alpha > 2$ the boundary does not simply adjust to the ambient pressure profile but instead asymptotes to a conical shape. This result is consistent with the expectation that in this case the transverse expansion time of the jet becomes shorter than the propagation time of magnetosonic waves across the flow, leading to a loss of causal connectivity and hence to a “free” ballistic expansion in a cone (Begelman et al. 1984; see also Section 5.4). This is essentially the behaviour exhibited by our Model E (see Fig. 11).

5.3.2 $\alpha = 2$

In this case the second term on the left-hand side of equation (54) is a positive constant. This implies that $1 < a \leq 2$. (Indeed, for $a > 2$, the third term diverges and hence unbalanced. For $a \leq 1$ it vanishes but the first term is non-negative and hence cannot balance the second one.) We can distinguish between the following two cases:

- $a = 2$ — the power law solution with $K^4 = C - 1/4$ is exact. This implies $C > 1/4$.
- $1 < a < 2$ — the third term becomes negligible at large Z and balancing of the first two terms requires $a \rightarrow 2/(1 + \sqrt{1 - 4C})$. This implies $C \leq 1/4$.

In other words, for $C < 1/4$ the centrifugal term is negligible and the resulting shape is $Z = (z_{1c}/r_{1c})x^{2/(1+\sqrt{1-4C})}$, whereas for $C > 1/4$ the centrifugal term is comparable to the other two terms and the solution is $Z = \sqrt{C - 1/4} x^2$. Fig. 20 verifies that the confining pressure in our simulated flows scales as Z^{-2} irrespective of the precise value of a so long as the shape exponent lies in the range $1 < a \leq 2$. The figure also corroborates the prediction that the Z^{-2} scaling is attained only gradually when $a < 2$ (models B and D, cor-

responding to $a = 3/2$) but that it is present almost from the start when $a = 2$ (model C).

As shown in Appendix A, the asymptotic solution for $C = 1/4$ is $x = Z^{1/2}(C_1 + C_2 \ln Z)$, where C_1 and $C_2 \neq 0$ are constants. (We kept the constant C_1 to accommodate the possibility that the solution extends all the way down to the light-cylinder radius, where $Z \approx 1$.) This solution is similar to the $C < 1/4$ solutions of equation (52) in having a negligible centrifugal contribution.

Although all the funnel shapes whose power-law indices lie in the range $1 < a \leq 2$ correspond to a single exponent ($\alpha = 2$) of the confining pressure distribution, there is nevertheless a one-to-one match between a given pressure distribution and the resultant funnel shape. This is because both the power-law index α and the magnitude of the confining pressure (as expressed in relation to the internal magnetic pressure at the light-cylinder radius by the parameter C ; see equation 49) play a role in determining the functional form of the boundary: when $C < 1/4$ the magnitude of C fixes the exponent of the boundary paraboloid, whereas when $C > 1/4$ it fixes the normalization constant K . The parameter C is evaluated at the effective base of the asymptotic region of the flow and it conveys physical properties (e.g. z_{1c} and Γ_{1c} ; see equation 49) imprinted on the outflow before it reaches the asymptotic regime. Thus, the asymptotic shape of a jet propagating through a power-law pressure distribution is determined both by the exponent of that distribution and by the evolution of the outflow before entering the asymptotic region.

5.3.3 $\alpha < 2$

In this case the second term on the left-hand side of equation (54) diverges as $Z \rightarrow \infty$. To balance this term, the third term must also diverge in this limit, which implies that $a = 4/\alpha > 2$ and $C = K^4$. Thus, the jet shape is paraboloidal, $Z = C^{1/\alpha}x^{4/\alpha}$. Like in the $\alpha = 2$ case, both the parameters α and C are needed to uniquely fix the functional form of the jet shape. For $\alpha = 4/3$ we have $a = 3$, the

funnel shape index of our numerical model F. Fig. 20 verifies that the boundary pressure for this model indeed scales as $Z^{-4/3}$.

We can collect the results derived in this subsection into a concise description of the correspondence between the exponent α of the ambient pressure distribution and the exponent a of the asymptotic jet shape:

- $\alpha < 2 \Leftrightarrow a = 4/\alpha > 2$,
- $\alpha = 2 \Leftrightarrow 1 < a \leq 2$,
- $\alpha > 2 \Leftrightarrow a = 1$.

Similar results for the behaviour of the ambient pressure in a confined jet ($\alpha \leq 2$) were found by Tchekhovskoy et al. (2008) in the force-free limit, which is consistent with the fact that our expressions for the spatial profile of Γ were obtained in effectively the same approximation.

As we have seen, $\alpha = 2$ leads to the asymptotic balance between the electromagnetic and poloidal curvature forces (regime iii) whereas $\alpha < 2$ leads to the balance between the electromagnetic and centrifugal forces (regime ii; see Section 5.2). These regimes are characterized by different evolution of many flow parameters, which may have observable consequences (see also Section 6). For example, in regime (ii) the product $\Gamma \tan \theta_v$ is predicted to be a constant $\mathcal{O}(1)$ in the acceleration region, whereas in regime (iii) it is expected to decrease with distance as $Z^{-(1-2/b)}$, with b being slightly larger than a due to the stronger collimation of the flow inside the jet. The evolution of the Lorentz factor in regime (ii) is given by $\Gamma \propto r$ (equation 38) rather than by the $\Gamma \propto r^{b-1}$ scaling of regime (iii). However, in practice this may not translate into a significant difference in how fast the jet accelerates (for example, $\Gamma \approx z^{1/3}$ for both the $\alpha = 4/3$ and $\alpha = 2$, $b = 3/2$ cases).

After the end of the acceleration the internal pressure scales as r^{-2} (since $\Gamma = \Gamma_\infty = \text{const}$). If the external pressure continues to decline as $z^{-\alpha}$, the pressure balance implies that the radial coordinate r increases faster compared to its variation during the acceleration. The new flow shape is $Z = C^{1/\alpha} \Gamma_\infty^{2/\alpha} x^{2/\alpha}$ as a result of equation (48). For example, in the cases $\alpha = 2$, $1 < a < 2$, the flow becomes radial and the opening angle of the jet remains constant. The quantity $\Gamma \tan \theta_v$ is also constant and equal to $C^{-1/2} = a/\sqrt{a-1}$ (using the relation between C and a , see Section 5.3.2). Thus, $\Gamma \tan \theta_v$ is a times larger compared to its value during the acceleration phase (see equation 43).⁶

5.4 Magnetic acceleration and causality

We have found that the acceleration efficiency is smaller when the wall has a conical shape (model A) than in the cases when its shape is paraboloidal (see Fig. 9). In the conical-wall case the flow attains equipartition only along field lines that are close to the rotation axis ($\Psi \leq 0.2\Psi_{\text{max}}$).

⁶ The change of this quantity is smooth and happens as the function $\Gamma(Z)$ changes from a power law to a constant. Equation (48), written as $x = C^{-1/2} Z^{\alpha/2} [\Gamma(Z)]^{-1}$, gives $\Gamma \tan \theta_v = \Gamma dx/dZ = C^{-1/2} (\alpha/2 - d \ln \Gamma / d \ln Z) Z^{\alpha/2-1}$. In the cases with $\alpha = 2$, $1 < a < 2$ the slope $d \ln \Gamma / d \ln Z$ changes from $1 - 1/a$ during the main part of the acceleration phase (see equation 41) to zero after it ends. As a result, $\Gamma \tan \theta_v$ changes from $1/\sqrt{a-1}$ to $a/\sqrt{a-1}$.

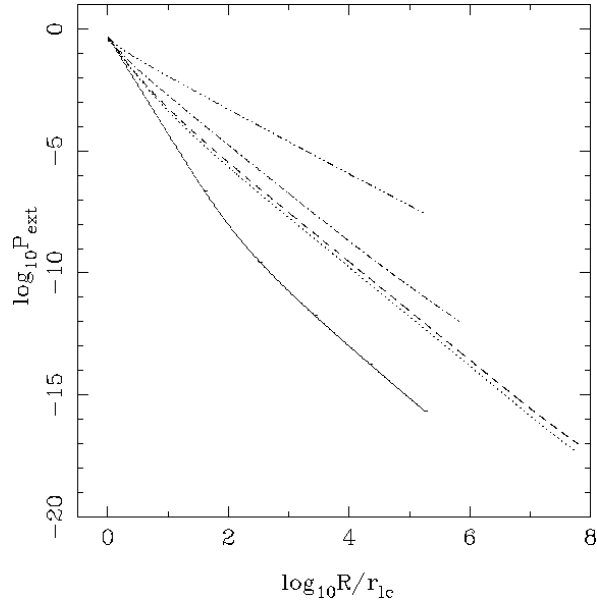


Figure 20. Evolution of total pressure along the jet boundary in models A (solid line), B1 (dashed line), C (dash-dotted line), D (dotted line) and F (dash-double-dotted line).

In accordance with our discussion in Section 5.1, the variation in the acceleration efficiency is tied to the difference in the degree of the collimation across the outflow, as seen in Fig. 16: Only for small values of Ψ does the exponent b become significantly larger than 1, corresponding to the innermost field lines bending toward the rotation axis, which implies that the bunching function \mathcal{S} decreases along this portion of the outflow. In order for collimation to occur, there must, however, exist causal connectivity across the outflow. A related discussion of this issue can be found in Zakamska et al. (2008). However, the simpler flow structure assumed in that paper excludes the possibility of magnetic acceleration. In particular, the assumption of zero azimuthal speed implies that the current I is a constant of motion (see equation 15), which in turn means that μ_m remains constant (see equation 20).

One can check whether the condition of causal connectivity is satisfied by comparing the field-line opening angle θ_v (defined in Section 5.2) with the half-angle of the Mach cone of fast waves, θ_m . The latter can be found from the relation

$$\sin \theta_m = \frac{\Gamma_f c_f}{\Gamma v_p}, \quad (55)$$

where c_f and Γ_f are the fast speed and the corresponding Lorentz factor, respectively. Since $\Gamma_f c_f = B_{\text{co}}/\sqrt{4\pi\rho}$, where B_{co} is the magnetic field as measured in the fluid frame, and $v_p \approx c$, we have

$$\sin \theta_m \approx \left(\frac{B_{\text{co}}^2}{4\pi\rho c^2} \right)^{1/2} \frac{1}{\Gamma} = \frac{\sigma^{1/2}}{\Gamma}. \quad (56)$$

In the magnetically dominated regime $\sigma \approx \mu/\Gamma$. For highly super-magnetosonic flows $\theta_m \ll 1$. Thus, we may write

$$\theta_m \approx \sqrt{\mu/\Gamma^3}. \quad (57)$$

In the hydrodynamic limit the fast magnetosonic speed re-

duces to the sound speed and Γ_f , c_f in equation (55) should be replaced by Γ_s , c_s . For the ultra-relativistic equation of state and $\Gamma \gg 1$ this gives $\theta_m \simeq 1/\Gamma$, the value used for causality analysis in Zakamska et al. (2008). However, in the magnetic case θ_m can be much higher because the magnetosonic speed can be much closer to the speed of light.

In the conical case we have $\Gamma \approx R/r_{lc}$, and

$$\theta_v/\theta_m \approx (\theta/\sqrt{\mu})(R/r_{lc})^{3/2} \quad (58)$$

grows rapidly to a value > 1 (where it is a good approximation to replace θ_v by θ). The left panel of Fig. 21 shows that only the inner part of the jet has $\theta_v/\theta_m < 1$ and thus in causal connection. Collimation (and thus efficient acceleration) is possible only in this inner region. In contrast, the outer parts of the conical jet lack causal connection with the axial region and the flow there is essentially ballistic.

In the paraboloidal case with $b < 2$ (for which $\theta_v \approx 1/\Gamma$ and $\Gamma \approx (R/r_{lc})^{(b-1)/b}$)

$$\theta_v/\theta_m \approx (\Gamma/\mu)^{1/2} \approx (1/\mu^{1/2})(R/r_{lc})^{(b-1)/(2b)}, \quad (59)$$

so this ratio grows much slower compared to the conical case. Moreover, the loss of causal contact formally occurs when $\Gamma \simeq \mu$, i.e. at the end of the acceleration phase. This is confirmed by our simulations. As one can see in the middle and right panels of Fig. 21, during the power-law acceleration phase θ_v/θ_m grows slowly but remains less than 1 almost everywhere in our numerical models. It subsequently decreases again when the growth rate of Γ goes down.

In contrast, in the paraboloidal case with $b > 2$ (for which $\theta_v \approx r/bz$ and $\Gamma \approx r/r_{lc}$),

$$\begin{aligned} \theta_v/\theta_m &\approx (1/b\mu^{1/2}C^{b/4})(r/r_{lc})^{(5/2)-b} \\ &= (1/b\mu^{1/2}C^{5/8})(R/r_{lc})^{(5/2b)-1} \end{aligned} \quad (60)$$

(see Section 5.3.3), and this ratio actually *decreases* with distance for $b > 5/2$! One can also argue quite generally that, even if Γ were to increase all the way up to μ , the value of the above ratio in that region, which can be estimated to be $\sim 1/b\mu^{b-2}C^{b/4}$, would likely remain < 1 (since $b > 2$, $\mu > 1$ and C is of the order of 1; see equation 49). Thus, the necessary (but not sufficient) condition for acceleration is satisfied in this case. This suggests that the acceleration efficiency may be comparable to the $1 \leq b < 2$ cases.

The behaviour of an unconfined wind is similar to that of an outflow in a conical funnel, which is not surprising given the fact that the former is a limiting case of the latter. As seen in Fig. 14, the acceleration in model AW is $\gtrsim 50\%$ efficient only along field lines that are close to the rotation axis ($\Psi \leq 0.1\Psi_{\max}$), similarly to the situation in model A.

5.5 Hot flows

When $w/\rho c^2$ is significantly larger than 1 at the inlet there is an additional reservoir of energy for the flow acceleration — the thermal energy of particles. As the flow expands the enthalpy per unit rest mass $w/\rho = c^2 + [s/(s-1)](p/\rho)$ (equation 11) decreases until it reaches its minimum value ($= c^2$), and beyond that point the flow can be regarded as cold. In the pure hydrodynamic case the thermal energy is directly transferred to the bulk kinetic energy of the fluid. In the magnetic case there is an additional possibility — the thermal energy can also be transferred to the Poynting flux.

Indeed, since $\mu c^2 = (w/\rho)\Gamma + \mu_m c^2$, it is possible to have both Γ and $\mu_m c^2$ increasing when w/ρ decreases, and this in fact is what we observe in model B2H (Fig. 13).

We have already noted in Section 5.1 that in Poynting flux-dominated flows μ_m is proportional to the bunching function \mathcal{S} (see equation 28). In agreement with this result, the left panel of Fig. 22 shows that in model B2H \mathcal{S} exhibits the same evolution as μ_m (which is shown in the middle panel of Fig. 13).

In the super-Alfvénic regime the trans-field force balance for hot flows is described by equation (32) even for hot outflows provided that p remains $\ll B_{co}^2/8\pi$. Therefore we still have $\mathcal{R} \sim \Gamma^2 r$ and hence $\Gamma \propto r^{b-1}$ along magnetic field lines of paraboloidal jets with exponents in the range $1 < b \leq 2$. Combining the mass conservation relation (13) and equation (29) we obtain

$$\Gamma\rho = \frac{k\Psi\mathcal{S}}{\pi r^2} \propto r^{-2},$$

where we took account of the fact that \mathcal{S} is a weak function of r . This enables us to write the variation of the thermodynamic parameters as

$$\rho \propto r^{-b-1}, \quad p \propto r^{-s(b+1)}.$$

In the limit $w \gg \rho c^2$ equation (11) gives $w \propto p \propto r^{-s(b+1)}$, and therefore $\mu_h = (w/\rho c^2)\Gamma$ scales as

$$\mu_h \propto r^\delta, \quad \delta = b(2-s) - s. \quad (61)$$

For model B2H with $b \approx 3/2$ and $s = 4/3$ this yields $\mu_h \propto r^{-1/3}$. Hence μ_h is expected to decrease and $\mu_m = \mu - \mu_h$ to increase along the field lines, in agreement with what is observed in the simulation.

Similar behaviour has been found in the self-similar solutions of Vlahakis & Königl (2003b), but only in cases where the flow is super-Alfvénic from the start (see also Vlahakis et al. 2003). In their trans-Alfvénic, hot-flow solutions (Vlahakis & Königl 2003a), μ_m remained constant throughout the thermal acceleration phase. This could be understood from the fact that these solutions corresponded to $b \approx 2$ and therefore to $\delta \approx 0$ in equation (61), resulting in constant μ_h and μ_m in the thermal acceleration region.⁷ In contrast, the super-Alfvénic solutions presented in Vlahakis & Königl (2003b) corresponded to $b \approx 3/2$ and hence to $\delta \approx -1/3$ (the same values as in our models B and D), and therefore they exhibited the same behaviour in the thermal acceleration zone as our simulated flows.

The increase of the Poynting-to-mass flux ratio μ_m in the thermal acceleration regime leads to a rather unusual behaviour of the azimuthal velocity. The right panel of Fig. 22 shows the variation of rv^δ along the same magnetic surface in models B2 and B2H. For the cold jet it always grows

⁷ As was shown analytically in the magnetodynamic self-similar solutions of Narayan et al. (2007), the field-line shape is $z \propto r^{2/(2-F)}$, where F is a constant parameter entering the self-similarity expression of the magnetic flux function, $\Psi = r^F \mathcal{F}(r/z)$. The MHD self-similar solutions follow the same scaling in their force-free regime. The trans-Alfvénic solutions presented in Vlahakis & Königl (2003a) were characterized by $F \approx 1$, which implies $b \approx 2$. Note in this connection that the $F = 1$ magnetodynamic solution is exactly the paraboloidal force-free solution presented by Blandford (1976).

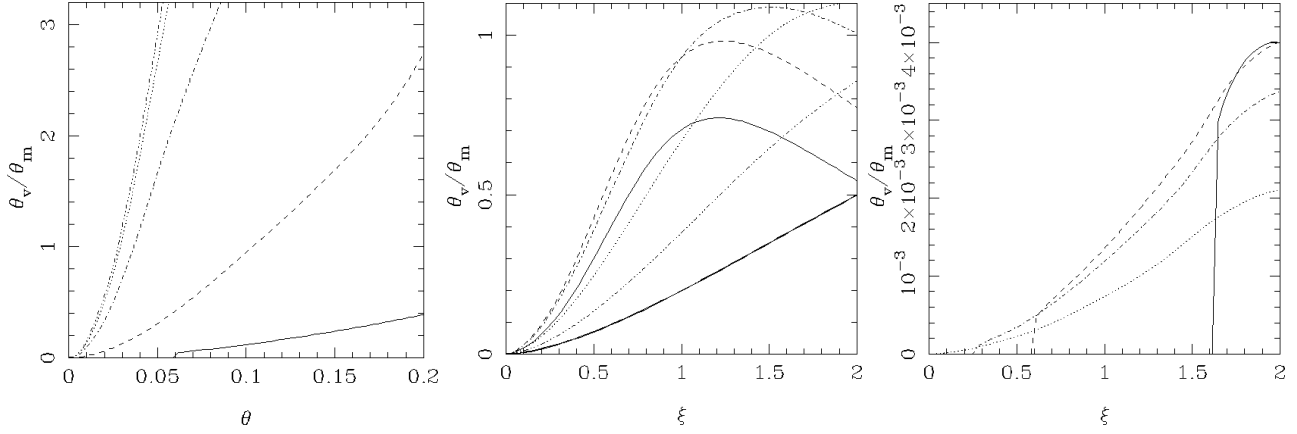


Figure 21. The ratio of flow half-angle, θ_v , to the Mach angle, θ_m , across the jet for models A (left panel), B3 (middle panel) and F (right panel). For model A the depicted cross-sections are at $R = 10$ (solid line), $R = 10^2$ (dashed line), $R = 10^3$ (dash-dotted line), $R = 10^4$ (dotted line) and $R = 10^5$ (dash-triple-dotted line). For model B3 the depicted cross-sections are at $\eta = 5 \times 10^2$ (thin solid line), $\eta = 5 \times 10^3$ (dashed line), $\eta = 5 \times 10^4$ (dash-dotted line), $\eta = 5 \times 10^5$ (dotted line), $\eta = 5 \times 10^6$ (dash-triple-dotted line) and $\eta = 5 \times 10^7$ (thick solid line). For model F the depicted cross-sections are at $\eta = 1.5 \times 10^3$ (thin solid line), $\eta = 5 \times 10^3$ (dashed line), $\eta = 1.5 \times 10^4$ (dash-dotted line), and $\eta = 1.5 \times 10^5$ (dotted line). The curves in the right panel dive to zero when the flow becomes sub-magnetosonic.

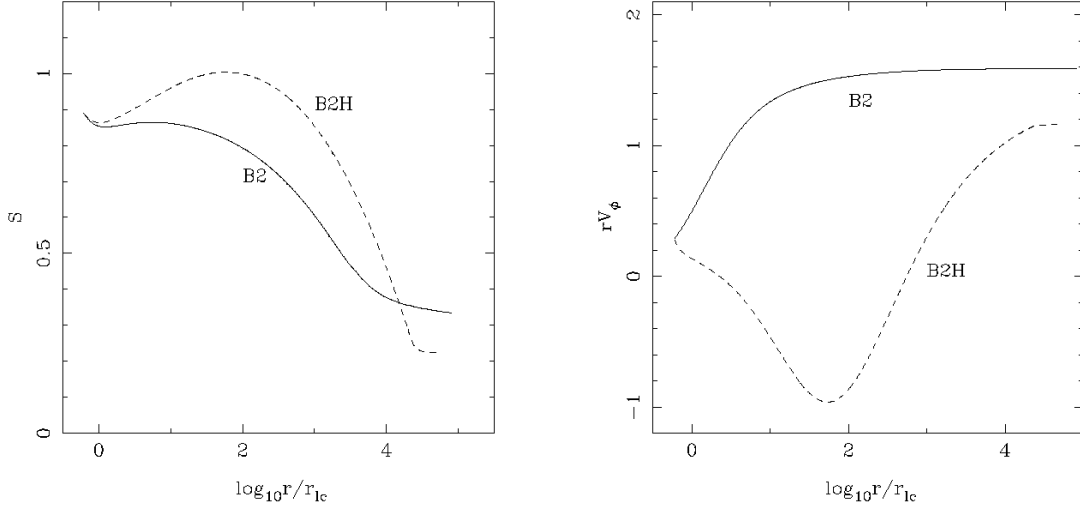


Figure 22. Effects of thermal acceleration. Left panel: the bunching function \mathcal{S} along the magnetic field line with $\Psi = 0.5\Psi_{\max}$. Right panel: $rv^{\hat{\phi}}$ along the magnetic field line with $\Psi = 0.5\Psi_{\max}$. Solid lines: model B2; dashed lines: model B2H.

with cylindrical radius and hence with the distance from the jet origin. This reflects the fact that the plasma is being spun up by the rotating magnetic field: in this case $|B_p/B^{\hat{\phi}}| \gg |v_p/v^{\hat{\phi}}|$ in equation (14) and $v^{\hat{\phi}} \approx r\Omega \propto r$. However, in the hot jet $rv^{\hat{\phi}}$ (and therefore also $v^{\hat{\phi}}$) initially decreases with increasing r and even attains negative values, indicating counter rotation of the plasma. Eventually the cold-jet behaviour is restored, with the switch taking place at the turning point of μ_m . The decrease in $rv^{\hat{\phi}}$ when μ_m increases along a field line follows from the following relation,

$$\frac{r\Omega v^{\hat{\phi}}}{c^2} = 1 - \frac{1 - l\Omega/\mu c^2}{1 - \mu_m/\mu}, \quad (62)$$

obtained by combining equations (15) and (16).⁸ Physically, the increase in μ_m implies that the magnetic contribution to the total angular momentum per unit rest mass goes up (see equations 20 and 15), which, by the conservation of l along a field line (and taking account of energy conservation) implies that the specific material angular momentum $rv^{\hat{\phi}}$ must decline.

The efficiency of the acceleration in model B2H is higher than in the cold models, as can be seen in Fig. 13. This is

⁸ The inequality $l\Omega/\mu c^2 < 1$ always holds in trans-Alfvénic flows, since $(l\Omega/\mu c^2)^{1/2}$ equals the value of r/r_{1c} at the Alfvén surface (e.g. Vlahakis & Königl 2003a), and the Alfvén surface is located closer to the source than the light cylinder (with the two surfaces almost coinciding for highly magnetized flows).

connected to the behaviour of the function \mathcal{S} . The increase of \mathcal{S} during the thermal acceleration phase results in a higher \mathcal{S}_f , the value of the function \mathcal{S} at the fast magnetosonic surface. In addition, the asymptotic value \mathcal{S}_∞ is smaller than in cold models (see Fig. 22). Both effects result in a higher value of Γ_∞/μ (see equation 31).

5.6 Comparison with semi-analytic solutions

As discussed in Section 1, it is possible to find exact solutions of the relativistic MHD equations by assuming radial self-similarity (Li et al. 1992; Contopoulos 1994; Vlahakis & Königl 2003a,b, 2004). Due to the mathematical complexity of the equations, these are the only possible exact semi-analytic solutions describing cold or polytropic flows (Vlahakis & Königl 2003a). Similarly to their non-relativistic counterparts (the Blandford-Payne-type models), they successfully capture the physics of magnetically driven jets and yield the general characteristics of the flow acceleration and collimation.⁹ In particular, the results of Vlahakis & Königl (2003a,b) for ultra-relativistic GRB jets follow the general scaling relationships derived here. In fact, the scaling $\Gamma \propto r^{b-1}$, corresponding to a streamline shape $z \propto r^b$ (for $1 < b \leq 2$; the regime (iii) of equation 37), was first presented in Vlahakis & Königl (2003b). Note in this connection that both the $\Gamma \simeq r/r_{1c}$ (equation 38) and the $\Gamma \simeq z/r$ (equation 41) scalings exhibited by our solutions could be captured through the basic radial-self-similarity ansatz $\Gamma = \Gamma(\theta)$ because both r/r_{1c} and z/r_{1c} are functions of the polar angle θ in the self-similar solutions. The semi-analytic solutions exhibit as high an acceleration efficiency ($\gtrsim 50\%$) as the simulated $b \leq 2$ solutions, and, correspondingly, have a similar value for the asymptotic shape function ($\mathcal{S}_\infty \sim 1/2$; Vlahakis 2004b). Self-collimation also acts in a similar way in both types of solution, with the inner field lines at any given height z being better aligned with the rotation axis than the poloidal field at larger values of r .

Despite their qualitative similarity in regard to the acceleration and collimation processes, the semi-analytic and numerical solutions do of course differ in their details, reflecting the fact that in the self-similar model the angular velocity at the base necessarily scales as $1/r$ and that only one current-flow regime is allowed. In particular, the spatial distributions of the integrals of motion is not the same in these two cases. For example, the energy integral, which is constant in the self-similar model, is roughly proportional to the magnetic flux function in the simulated uniform-rotation jets, and the adiabat Q , which is given as a power of the magnetic flux function in the self-similar model, is a global constant in the simulations. We also note that, while the far-asymptotic (beyond the acceleration region) flow shape in the self-similar models is either cylindrical or conical, only the innermost field lines become cylindrical in the simulated jets, whereas further out the streamlines remain paraboloidal. However, this is evidently related to the imposed boundary shape, and we can expect that, if the flow were followed to still larger distances, even more of the

⁹ The self-similar solutions of Vlahakis & Königl (2003a) have a line-shape $z \propto r^2$ (see footnote 7) and thus most closely resemble our model C.

interior field lines would tend to cylinders (see Chiueh et al. 1991) or (in the case of an initially “hot” flow) to cones.

The high acceleration efficiency inferred from the self-similar and numerical solutions for non-radial, relativistic MHD outflows was also deduced by Beskin & Nokhrina (2006) on the basis of a perturbative analysis around a parabolic ($z \propto r^2$) flow. These authors found that the Lorentz factor increases with distance from the origin as $\Gamma \propto z^{1/2}$, in agreement with our general result for paraboloidal jets of this type, $\Gamma \sim z/r$.

6 APPLICATION TO GRB JETS

The observational study of GRBs has not yet reached the stage where the basic parameters of the flows producing prompt γ -ray emission and afterglows have become well established. There is no general consensus yet on the angular structure, degree of collimation, distance from the central source or composition of GRB jets. These parameters may vary significantly from burst to burst. The anisotropy of γ -ray emission due to relativistic beaming further complicates the problem as the same burst could have a very different appearance when observed from different viewing angles. In this section we test our theory against the current, not yet very stringent, observational constraints and provide a guide for future observations.

The maximum terminal Lorentz factors in our numerical models of parabolic jets, $\sim 100 - 300$, are close to those inferred for long/soft GRB jets and also high enough to ensure that we have captured the properties of magnetic acceleration in the ultra-relativistic regime. Although real GRB jets may be even faster (e.g. Lithwick & Sari 2001), the analytic results verified by our numerical study can be applied to such jets with a high degree of confidence.

To make detailed comparisons between our theory and the observations we need to determine the characteristic light-cylinder radius at the source of the jets. In the case of a millisecond magnetar

$$r_{1c} = \frac{cT}{2\pi} \simeq 5 \times 10^6 \left(\frac{T}{1 \text{ ms}} \right) \text{ cm},$$

and for a maximally rotating black hole

$$r_{1c} = 4r_g \approx 6 \times 10^5 \left(\frac{M}{M_\odot} \right) \text{ cm}.$$

Thus, $L = 10^6 \text{ cm}$ is a suitable reference length-scale for this application.

Given the extended nature of magnetic acceleration, the first question that one has to address is whether the Lorentz factors deduced from observations can be reached in our model on the inferred scale of the γ -ray emission region. According to equations (38) and (42),

$$R \simeq 10^{12} \left(\frac{\Gamma}{100} \right)^3 \text{ cm}$$

for paraboloidal jets with $b = 3/2$ and $b = 3$, and

$$R \simeq 10^{10} \left(\frac{\Gamma}{100} \right)^2 \text{ cm}$$

for paraboloidal jets with $b = 2$. These estimates are lower than the distance to the γ -ray production region inferred

from the burst variability in the internal-shocks model of GRBs,

$$R_\gamma \sim \Gamma^2 c \delta t = 3 \times 10^{13} \left(\frac{\Gamma}{100} \right)^2 \left(\frac{\delta t}{0.1 \text{ s}} \right) \text{ cm},$$

where δt is the internal variability time-scale (e.g. Piran 2005). In fact, recent *Swift* observations indicate even larger distances ($\sim 10^{15} - 10^{16}$ cm; e.g. Lyutikov 2006a; Kumar et al. 2007). The theory thus appears to be consistent with the observations in this respect.

We emphasize that the above results have been derived in the context of ideal and axisymmetric MHD. In reality, various instabilities, and in particular non-axisymmetric, current-driven ones occurring near the jet axis, may result in magnetic reconnection and dissipation. It is interesting to note in this connection that the dissipation of Poynting flux would naturally generate a negative magnetic pressure gradient (associated with the azimuthal field component) along the flow and that this process was argued to be capable, on its own, to accelerate the flow to a high Lorentz factor (e.g. Drenkhahn & Spruit 2002; Drenkhahn 2002). In this respect our ideal-MHD simulations may be yielding only lower limits on the terminal Lorentz factor in the modelled jets.

A related issue is whether there is an adequate confining medium, as required for the establishment of the “power-law” acceleration regime described by equation (42). If the confinement of a long/soft GRB jet is provided only by the envelope of the progenitor massive star, as proposed by Tchekhovskoy et al. (2008), the acceleration would need to take place on a scale smaller than the stellar radius, $\sim 10^{11} - 10^{12}$ cm. Downstream of the stellar surface the jet is expected to enter the regime of “free” (ballistic) expansion, as in our model E, which is characterized by a less efficient magnetic acceleration.¹⁰ But even this rather restrictive constraint on the size of the acceleration region, and hence on Γ_∞ , is in principle consistent with the theory. An alternative possibility is that the GRB outflow is confined by a wind launched from the surface of a disc that surrounds the central object (e.g. Levinson & Eichler 2000). This mechanism is a prime candidate for the confinement of short/hard GRB outflows, which evidently do not originate inside a star. In this case the collimation might be attained smoothly, with the disc-driven and central object-driven components constituting parts of a coherent outflow configuration (e.g. Tchekhovskoy et al. 2008). However, the outflow may also involve shocks formed at the interface of these two components (e.g. Bromberg & Levinson 2007). If the GRB jet and disc outflow commence at the same time,

¹⁰ It has been suggested that matter-dominated GRB jets could remain confined by the expanding cocoon of relativistically hot shocked jet material after they break out through the stellar surface (e.g. Ramirez-Ruiz et al. 2002) and could continue to accelerate during that phase (e.g. Lazzati & Begelman 2005). In contrast, Poynting-dominated jets do not inflate large cocoons but instead create the so-called “nose cones” (e.g. Komissarov 1999b). In fact, given the low compression ratio of a fast shock in a magnetically dominated plasma, a jet termination shock is unlikely to form before the jet emerges from the star — instead, the jet would have the form of a super-Alfvénic but sub-fast-magnetosonic outflow, as has been observed in recent computer simulations (e.g. Komissarov & Barkov 2007; Barkov & Komissarov 2008).

the spatial extent of the confining medium in this picture can be estimated as

$$R_{\text{wind}} \approx 3 \times 10^9 \left(\frac{v_{\text{wind}}}{0.1 c} \right) \left(\frac{\Delta t}{1 \text{ s}} \right) \text{ cm},$$

where v_{wind} is the mean wind speed over this distance and Δt is the GRB duration (normalized here to a fiducial value appropriate for a short/hard burst). This should be compared with the above theoretical relationships between R and Γ , which for $\Gamma = 30$ (a fiducial value for the lower limit on Γ_∞ in short/hard GRBs; e.g. Nakar 2007) yields $R \approx 3 \times 10^{10}$ cm for $b = 3/2$ or $b = 3$ and $R \approx 9 \times 10^8$ cm for $b = 2$. This comparison indicates that, over the time Δt , a moderately relativistic disc outflow could form a sheath around the jet acceleration region. Given that the size of a disc that forms during a binary (NS-NS or NS-BH) merger that gives rise to a short/hard GRB event is not expected to exceed a few times 10^6 cm (i.e. significantly less than the expected cylindrical radius of the jet in the main acceleration region), meaningful confinement would be attained only if the wind had sufficiently large inertia, which would require the wind-to-jet total energy ratio to be $\gg 1$ (cf. Levinson & Eichler 2000). If the initial magnetizations of short/hard and long/soft GRB outflows are comparable, this scenario provides a plausible explanation of the finding (from the best available current data) that short-GRB jets are on average less relativistic than their long-duration counterparts. A concomitant prediction, which could be tested when more afterglow data for short/hard GRBs become available, is that short/hard GRB outflows should also be less well collimated, on average, than long/soft ones.

The internal-shocks model envisions the prompt GRB emission to be powered by the collision of successively ejected relativistic “shells” (e.g. Piran 2005). This scenario requires the jet to be kinetic

energy-dominated on the scale of the emission region; otherwise, the flow deceleration and dissipation at fast shocks is too weak (or else, if the flow is inhomogeneous, the energy requirements are strongly increased). The numerical solutions presented in this paper have demonstrated the possibility of efficient conversion of Poynting flux into bulk kinetic energy, with $\gtrsim 50\%$ efficiency attained by the end of the power-law-like acceleration regime. However, the distance R_γ of the prompt emission region from the central source imposes a constraint on the initial magnetization of GRB jets in this model. Using equation (45), we obtain

$$\mu \approx 2\Gamma_\infty < \begin{cases} 2(r_\gamma/r_{1c})^{b-1} & \text{if } b \leq 2 \\ 2(r_\gamma/r_{1c}) & \text{if } b \geq 2 \end{cases}. \quad (63)$$

For paraboloidal jets with $b = 3/2$ or $b = 3$ this gives (setting $R_{1c} \approx r_{1c}$)

$$\mu < 430 \left(\frac{R_\gamma}{10^{13} \text{ cm}} \right)^{1/3},$$

whereas for $b = 2$ we obtain

$$\mu < 6 \times 10^3 \left(\frac{R_\gamma}{10^{13} \text{ cm}} \right)^{1/2}.$$

By approximating $\Gamma_\infty \dot{M}_j c^2 \approx \mathcal{E}/\Delta t$, where \mathcal{E} the outflow kinetic energy as inferred from afterglow observations and Δt is the burst duration, we estimate the mass outflow rate

in the jet to be

$$\dot{M}_j \approx 5.6 \times 10^{-8} \left(\frac{\mathcal{E}}{10^{51} \text{erg}} \right) \left(\frac{\Delta t}{10 \text{s}} \right)^{-1} \left(\frac{\Gamma}{10^3} \right)^{-1} M_\odot \text{s}^{-1},$$

where we normalized by values appropriate to long/soft bursts. This is very much lower than the expected mass accretion rate onto the central black hole in the collapsar model ($\sim 0.05 - 1 M_\odot \text{s}^{-1}$; e.g. Popham et al. 1999) and constitutes the so-called ‘‘baryon loading problem’’ in GRB source models. Such a comparatively low mass outflow rate might be produced if the GRB-emitting outflow originates on magnetic field lines that thread the horizon of a spinning black hole and tap its rotational energy via the Blandford-Znajek mechanism (e.g. Levinson & Eichler 1993); in this case the flow would initially be baryon-free and would require a baryon-injection mechanism as it propagates outward. Alternatively, jets launched from an accretion disc may experience such a low mass loading if they are initially thermally driven along magnetic field lines inclined at a small ($\lesssim 15^\circ$) angle to the rotation axis (Barzilay & Levinson 2008).¹¹

The internal-shocks model of GRBs has been questioned on account of the relatively high emission efficiency that it requires, and these challenges have become significantly stronger following observations made by *Swift* (e.g. Granot et al. 2006; Kumar et al. 2007). Various suggestions have been made (and continue to be made) in the literature for reconciling this scenario with the observations (e.g. Kobayashi & Zhang 2007) or else for modifying or replacing it. Perhaps the main alternative picture proposed to date is based on the assumption that the prompt high-energy emission is produced directly from the dissipation of magnetic energy without requiring it to be converted into kinetic energy first (e.g. Kumar et al. 2007), which circumvents the efficiency problem that has troubled the internal-shocks model. Although magnetic dissipation could in principle occur also in the context of the MHD model (e.g. Drenkhahn & Spruit 2002), perhaps the most extreme realization of this idea occurs within the framework of the magnetodynamics scenario, in which GRB outflows are regarded as remaining Poynting flux-dominated (and sub-fast-magnetosonic) in the γ -ray emission region (e.g. Blandford 2002; Lyutikov 2006b). In this scenario, neither the internal nor the reverse shocks of the standard model would develop, which could be the basis for an observational test.¹²

As we discussed in Section 5.2, a key prediction of the magnetic acceleration model is the approximate inverse pro-

portionality between the Lorentz factor along a poloidal magnetic surface and $\tan \theta_v$ for that surface for paraboloidal jets with $1 < b \leq 2$ (see equation 43). For a small opening angle and b not very close to 1 this result can be approximated as $\Gamma \theta_v \approx 1$. This implies that GRB outflows with $b \leq 2$ that attain $\Gamma \sim 100$, the approximate inferred lower limit for long/soft GRBs, must have $\theta_v \sim 0.6^\circ$, essentially independent of the details of the acceleration process. When $b > 2$, $\Gamma \theta_v \approx b^{-1} (R/r_{lc})^{-(1-2/b)}$ decreases with R in the magnetic acceleration region, implying an even smaller value of θ_v at the end of this zone. The relation $\Gamma \theta_v \sim 1$ may be useful for differentiating between magnetic and fireball models of GRB flows. Indeed, this property is generic to the magnetic acceleration mechanism, whereas for the thermal acceleration the terminal bulk Lorentz factor is essentially given by the thermal Lorentz factor at the base of the flow and is fairly independent on the flow collimation, which means that the product $\Gamma \theta_v$ can in principle become $\gg 1$. Interestingly, one of the proposals made for interpreting the apparent GRB ‘‘tails’’ observed by *Swift* invokes a GRB-emitting outflow component whose opening half-angle must be $< 1^\circ$ (Panaitescu 2007). While the currently available data are not sufficient for favouring this interpretation over other suggested explanations of the ‘‘tails,’’ it is noteworthy that the requirement arrived at by Panaitescu (2007) on strictly phenomenological grounds is consistent with a distinguishing property of the magnetic acceleration model. It is also noteworthy that there is already at least one source (GRB 070401) in which such a small opening half-angle has been inferred directly from a measurement of an early break in the X-ray afterglow light curve (Kamble et al. 2008). Such small asymptotic opening angles and even $\Gamma \theta_v \lesssim 1$ could in principle be attained also in purely hydrodynamical jet models, although this would require a very high efficiency of collimation and acceleration within the stellar interior. Specifically, the jets would need to emerge from the star with $\theta_v < 1^\circ$ and $\Gamma \gtrsim 1/\theta_v \simeq 60$, which, in view of recent analytic and numerical studies (e.g. Lazzati & Begelman 2005; Morsony et al. 2007), is unlikely to be achieved in practice.

The original fireball model for GRB jets envisions a uniform conical outflow that becomes accelerated to Lorentz factors $\Gamma \gg 1/\theta_v$ and predicts that during the afterglow phase the Lorentz factor of the forward shock driven by the jet into the ambient medium will decrease to values $< 1/\theta_v$. The observational consequence of this transition is a panchromatic break in the afterglow light curve (referred to as the ‘‘jet break’’) occurring when $\theta_v \Gamma$ becomes ~ 1 (e.g. Rhoads 1999; Sari et al. 1999). In view of the results presented in this paper, the predictions of the MHD model for GRB outflows that are efficiently accelerated — and therefore necessarily confined (by either thermal, magnetic or ram pressure) during the acceleration phase — are radically different. Specifically, the MHD model predicts that the afterglow light curve would exhibit either a very early jet break (in cases where $\Gamma \theta_v \approx 1$ at the end of the acceleration phase, as expected in jets with $b \leq 2$) or no jet break at all (if $\Gamma \theta_v < 1$ at the end of the magnetic acceleration region, as expected in jets with $b > 2$).¹³ This prediction is seemingly

¹¹ It was also proposed that the problem could be alleviated in a magnetically driven disc outflow that is initially neutron rich and hot if the neutrons decouple from the protons well before the latter attain their terminal Lorentz factor (see Vlahakis et al. 2003 and Fuller et al. 2000). There are indications from studies of discs around non-rotating black holes that this might not work in practice because outflows may be required to be comparatively massive to remain neutron rich (e.g. Levinson 2006; Barzilay & Levinson 2008), but this conclusion still needs to be verified in the case of discs around rapidly rotating black holes.

¹² Note in this connection that, in some of the proposed interpretations of the *Swift* data (e.g. Uhm & Beloborodov 2007; Genet et al. 2007), the entire afterglow emission is attributed to a reverse shock that is driven into the ejecta.

¹³ If the low current detection rate of jet breaks in the early afterglow light curves of GRB sources would prove to be more

at odds with the inference from a number of pre-*Swift* GRB sources of breaks of this type occurring on a time-scale of days (see e.g. Liang & Zhang 2005 for a compilation). The paucity of “textbook” jet breaks in *Swift* GRB sources (e.g. Liang et al. 2008), which has even cast doubts on the interpretation of the alleged pre-*Swift* jet breaks, points to one way out of this dilemma: it may be that indeed there are no bona fide jet breaks at later times. We recall, however, that the jet-break interpretation lies at the basis of the identification of GRB outflows as collimated jets, which has significantly reduced the otherwise prohibitive energy requirements in some sources. Alternatively, it could be that the difficulties in finding late-time jet breaks in *Swift* sources are to a large extent observational (e.g. Zhang 2007), in which case other explanations for late-break candidates must be sought.

One natural possibility is that the outflow possesses more than one kinematic component. In its simplest incarnation, this is the “two component” model, which envisions the prompt emission to originate in an ultra-relativistic, highly collimated jet and the afterglow emission to be dominated by a less relativistic, wider outflow component. The suggestion in Panaitescu (2007) and in Kamble et al. (2008) that the γ -ray emitting jet is very narrow was made in the context of this model, and a similar picture was used by Granot et al. (2006) to explain other aspects of the early GRB X-ray emission measured by *Swift* (see also Zhang 2007). In fact, a two-component outflow configuration had already been proposed in the pre-*Swift* era to account for certain observations (e.g. Berger et al. 2003b) and as a means of alleviating the efficiency requirements on the internal-shocks model (Peng et al. 2005). The separation into two components could arise either from an interaction of the outflow with the envelope of a massive progenitor star or represent an intrinsic property of the central engine (see Peng et al. 2005 for a summary of some specific proposals). In the context of the magnetically driven outflow model, there are at least two possibilities for an intrinsic origin. First, neutron-rich, hot outflow may split into two components when the neutrons and protons decouple before the protons have attained their terminal Lorentz factor (Vlahakis et al. 2003). Second, a baryon-poor ultra-relativistic outflow launched from the black hole can be surrounded by a magnetically driven, relativistic outflow from the accretion disc itself (see Granot et al. 2006).¹⁴ We stress that, in reality, the outflow may be more complex than in the schematic “two component” picture sketched above. For example, inhomogeneities in the accretion flow may result in several distinct outflow components emerging from the disc, associated, perhaps, with isolated magnetic flux tubes that thread the disc at different locations. Phenomenologically, this situation might resemble the “patchy shell” scenario considered by Kumar & Piran (2000).

The distribution of the terminal Lorentz factor and of

the kinetic power across the jet directly affects the evolution of the light curve of the GRB afterglow (e.g. Granot 2005) as well as the statistical properties of a GRB sample (e.g. Nakar et al. 2004) and the detectability of “orphan” afterglows (afterglows detected without an associated GRB; e.g. Nakar & Piran 2003). One could in turn attempt to use such observations to probe the jet structure and to test the underlying acceleration and collimation models. With this in mind, we present in Fig. 23 illustrative asymptotic distributions of the Lorentz factor and of the kinetic power from our simulations.

We consider first the Γ_∞ distribution. The top left panel of Fig. 23 shows that in all of the cases the Lorentz factor decreases toward the axis — this is a generic feature of the axisymmetric, ideal-MHD acceleration mechanism as the azimuthal magnetic field and hence the Poynting flux vanish along the symmetry axis. This feature may not, however, be as pronounced when non-axisymmetric instabilities and resistive dissipation of magnetic energy (which are not incorporated into our study) are taken into account. In fact, we find that even in our solutions $\Gamma \neq 1$ at $\theta = 0$ because of numerical dissipation. In the case of an initially hot outflow $\Gamma(\theta = 0) > 1$ is due to the thermal acceleration. In initially cold outflows that have uniform rotation and mass density distribution at the base Γ peaks at the jet boundary. It is seen, however, that if the flow is initially hot the anisotropy of the Lorentz factor distribution within the jet is reduced. Uniform rotation is a robust prediction of models with a magnetar or a magnetized black hole as a central rotator. The assumption a uniform mass-flux distribution at the jet base is more of an approximation: for example, when the central source is a black hole the degree of baryon loading is likely to be higher near the jet boundary due to various boundary interactions with the jet surroundings (e.g. Levinson & Eichler 2003). Such a mass distribution would lead to lower terminal Lorentz factors near the boundary compared to that found in our simulations. If the inner regions of an accretion disc contribute to the magnetic driving of the GRB-emitting outflow component then a model with differential rotation, with Ω decreasing away from the centre, is more suitable. As seen from the figure, in this case the terminal Lorentz factor peaks at intermediate angles. In practice it may, however, be difficult to distinguish this case from that of uniform rotation with nonuniform mass loading.

Turning now to the distribution of energy flux across the jets in the asymptotic regime, we recall that the observational consequences of this energy are strongly influenced by relativistic beaming — whenever a fraction of this energy is dissipated and converted into radiation, this radiation will be beamed in the direction of motion of the corresponding fluid element, given by θ_v . Most phenomenological models of GRBs have assumed that the jet is conical and has radial streamlines. Thus, the streamline angle, θ_v , is equal to θ , the polar angle of the fluid element. In our model the streamlines are curved and asymptotically their shape is close to that of the boundary (with the exception of the cylindrical core). Hence we have $\theta_v \simeq \theta/a$. Consider a surface element normal to the η coordinate lines (streamlines) $d\Sigma_\eta = \sqrt{g_{\phi\phi}g_{\xi\xi}}d\phi d\xi$, where $g_{\phi\phi}$ and $g_{\xi\xi}$ are components of the metric tensor. Since in the asymptotic regime $\theta, \theta_v \ll 1$, we can write $d\xi = az^{1-1/a}d\theta_v$, $g_{\phi\phi} = r^2$ and $g_{\xi\xi} = z^{2/a}$ (see

than just the result of observational difficulties, this could be an indication, when interpreted in the context of the magnetic acceleration model, that these jets are characterized by effective shape-function exponents $b > 2$.

¹⁴ In the latter scenario, the disc wind could provide a ready source for seeding the central funnel with baryons (e.g. Levinson & Eichler 2003) and could also help collimate the interior outflow (Levinson & Eichler 2000).

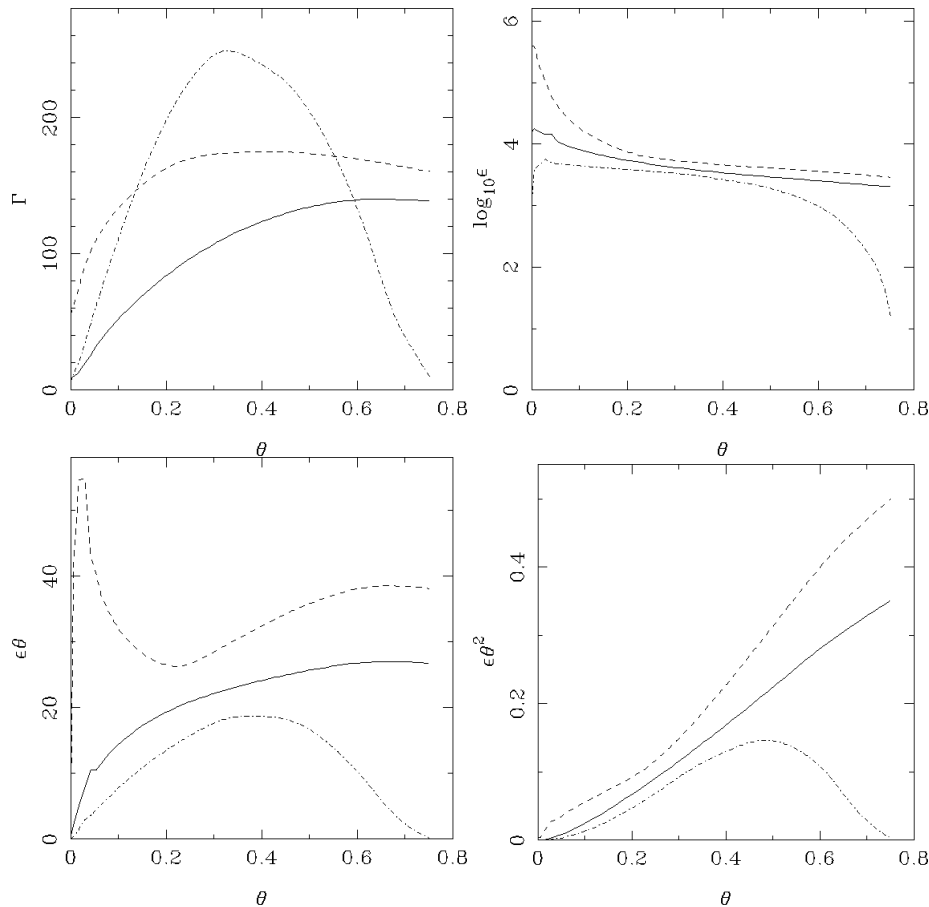


Figure 23. Angular distributions of the Lorentz factor (top left panel), the kinetic power per unit solid angle in the local direction of the flow (ϵ , top right panel), the kinetic power per annulus of unit angular size ($\epsilon\theta$, bottom left panel) and $\epsilon\theta^2$ (bottom right panel) in the asymptotic regime, plotted as functions of polar angle. The variable ϵ is given in units of $cB_0^2 L^2/4\pi$, and when it is multiplied by θ or θ^2 the polar angle is measured in radians. Note, however, that the polar angle along the horizontal axis is given in degrees. The solid lines show model B2, the dashed lines model B2H, and the dash-dotted lines model D.

Appendix A of Paper I), and hence

$$d\Sigma_\eta = a^2 z^2 d\omega,$$

where $d\omega = \theta_\nu d\theta_\nu d\phi$ is the solid angle defined by the tangents to the streamlines passing through the surface element. The power per unit solid angle is then given by

$$d\mathcal{L}/d\omega \equiv \epsilon = S^\eta a^2 R^2,$$

where S^η is the component of the energy flux density in the η direction.

The top right panel of Fig. 23 shows the distribution of kinetic power per unit solid angle, ϵ (the total power has a very similar distribution). One can see that in all models it peaks at, or very close to, $\theta = 0$. The reason for this behaviour, which seemingly conflicts with the Lorentz factor distribution shown in the left panel of the figure, is that the density distribution across the jet is highly nonuniform, with the mass density strongly peaking near the symmetry axis on account of the enhanced collimation of the flow in that region (see Figs. 2–5). The bottom left panel of Fig. 23 shows the distribution of $\epsilon\theta$; this quantity tells us how the jet power is distributed between annuli of equal size in θ . One can see that in model D (differential rotation) more power comes from the intermediate annuli, in model B (uniform rotation

at the base) from the outer annuli, and that a significant core component emerges in model B2H (initially hot jet). Note, however, that the distributions of the Lorentz factor and the power depend on the choices of the density, magnetic flux and angular velocity distributions at the inlet boundary, so different profiles may be possible.

The derived distributions of $\Gamma(\theta)$ and $\epsilon(\theta)$ are markedly different from those commonly adopted in phenomenological GRB jet models, which either take them to be uniform within the jet half-opening angle θ_j or else assume that the flow has a universal structure, with ϵ being a Gaussian or a power-law in θ (in particular, $\epsilon \propto \theta^{-2}$; Rossi et al. 2002 — compare with the bottom right panel of Fig. 23) outside a uniform-core region.¹⁵ The structure exhibited by our

¹⁵ In the force-free electromagnetic model for GRBs it is envisioned that the current flows along the axis of rotation and returns through the equatorial plane; this yields an energy distribution $\propto \theta^{-2}$ in the associated electromagnetic shell (e.g. Blandford 2002; Lyutikov 2006b). A universal structured outflow with $\epsilon \propto \theta^{-2}$ could potentially also be produced when a relativistic GRB jet with possibly a different initial energy distribution breaks out through the surface of a massive progenitor star (Lazati & Begelman 2005).

model jets is also different from that of a “hollow cone,” where the flow occupies the region $\theta \in [\theta_j - \Delta\theta, \theta_j]$ (e.g. Eichler & Levinson 2004; Lazzati & Begelman 2005). Although the distribution of Lorentz factors is reminiscent of such a cone, the distribution of kinetic power actually peaks near the symmetry axis. Moreover, in contrast with the phenomenological hollow-cone models considered in the literature, in which $\Delta\theta \ll \theta_j$, our solutions yield configurations with $\Delta\theta \sim \theta_j$. The detailed observational implications of these structures remain to be explored.

7 CONCLUSION

In this paper we extend our previous numerical study of magnetically accelerated relativistic jets (Paper I) from the case of terminal Lorentz factors $\Gamma_\infty \sim 10$, appropriate to AGN jets, to $\Gamma_\infty \gtrsim 10^2$, appropriate to GRB jets. The larger values of Γ_∞ reached in the present study enable us to compare results of our simulations, carried out using the equations of special-relativistic ideal MHD, with the asymptotic analytic formulae that we obtain from the constituent equations in the limit $\Gamma \gg 1$. Our analysis of the results also benefits from a comparison with semi-analytic solutions that were derived under the assumption of radial self-similarity. We can summarize our conclusions regarding the magnetic acceleration of ultra-relativistic outflows as follows.

(i) Our simulations verify that the MHD acceleration mechanism remains robust even when the terminal Lorentz factors reach the ultra-relativistic regime ($\Gamma_\infty \gtrsim 10^2$). The simulated flows rapidly settle into quasi-steady and seemingly stable configurations. A complete model would need to incorporate non-axisymmetric effects, which we have not considered.

(ii) A key property of magnetically driven relativistic flows in the ideal-MHD regime is the spatially extended nature of their acceleration. This property, which was first revealed by the self-similar solutions and subsequently confirmed in the moderately relativistic regime by the simulations reported in Paper I, is also a distinguishing characteristic of jets accelerated to ultra-relativistic speeds. For initially Poynting flux-dominated jets whose magnetic flux surfaces can be approximated by paraboloids of the form $z \propto r^b$ (with $b \geq 1$), the Lorentz factor during the main magnetic acceleration phase increases as $\Gamma \simeq (b/\sqrt{b-1})z/r$ when $1 < b \leq 2$ and as $\Gamma \simeq r/r_{1c}$ when $b = 1$ or $b > 2$. After the (increasing) kinetic energy flux becomes comparable to the (decreasing) Poynting flux the growth of Γ saturates, and thereafter it increases at a much slower rate. (We have not been able to reach this phase in models with $b > 2$ due to the limitations of our numerical method.)

(iii) The conversion efficiency Γ_∞/μ of total injected energy to kinetic energy at the end of the power-law acceleration phase lies in the range 55 – 75% for the initially cold simulated paraboloidal flows whose effective exponents lie in the range $1 < b \leq 2$; the efficiency is smaller the larger the initial magnetization (or, equivalently, the higher the value of Γ_∞). A higher efficiency is attained in jets with $b < 2$ that are initially relativistically hot than in the corresponding initially-cold outflows: in this case a measurable fraction ($> 50\%$ in the example that we show) of the thermal energy

flux is at first converted into Poynting flux, thereby reducing the initial thermal acceleration of the flow and enhancing the subsequent magnetic acceleration.

(iv) In our simulations the flow is confined by a rigid wall whose shape is described by $z \propto r^a$, with a ranging from 2/3 to 3. We have conducted a detailed analytic investigation of the relationship between a confining pressure distribution of the form $p_{\text{ext}} \propto z^{-\alpha}$ and the shape of the jet boundary in the asymptotic regime of the magnetic acceleration zone. We found that there is a one-to-one correspondence between the functional forms of the pressure distribution and of the boundary shape. Except for one special case (for which a remains close to 2), the jet becomes an exact paraboloid of the form given above, with $a = 4/\alpha > 2$ for $\alpha < 2$ and $1 < a \leq 2$ for $\alpha = 2$. When $\alpha > 2$ the jet cannot maintain pressure equilibrium with the ambient medium and asymptotes to a conical shape. This situation is reproduced in our simulations by unconfined flows as well as by flows with $a \leq 1$. In this case the outer regions of the jet become causally disconnected (the local opening half-angle of the field lines becomes larger than the local half-angle of the Mach cone of fast-magnetosonic waves), and only the innermost regions continue to collimate and accelerate.

(v) We find that for all current-carrying jets (irrespective of whether the return current flows inside or outside the jet) the innermost field lines are more strongly collimated than the exterior ones, indicating “self collimation” by the magnetic hoop stress (see also Paper I). This redistribution of the poloidal field lines within the jet is directly responsible for the high acceleration efficiency of the flow.

We have applied our results to GRB sources, taking into account the constraints imposed by the detected prompt and afterglow emission on the properties of the ultrarelativistic jets that evidently give rise to the GRB phenomenon. Our main conclusions are:

(i) Initially Poynting flux-dominated outflows can be magnetically accelerated to a Lorentz factor exceeding the minimum ($\Gamma \sim 10^2$) inferred in long/soft GRBs within a distance of $\sim 10^{11} - 10^{12}$ cm from a rapidly rotating stellar-mass black hole or a millisecond magnetar. Thus, most of the acceleration of long/soft GRB jets can be achieved inside a typical progenitor star in the collapsar model, whose envelope provides a natural confining environment for the jets. Lack of confinement outside of the star may result in a radial outflow characterized by loss of causal connectivity across the jet and inefficient acceleration. An alternative confinement mechanism that is of particular relevance to short/hard GRBs, which likely form through a merger of compact stars rather than in the collapse of a massive star, is a disc wind. The MHD acceleration mechanism implies that the minimum bulk Lorentz factor inferred in short/hard GRBs ($\Gamma \sim 30$) could be attained within the distance that such a wind covers over the burst duration if the disc outflow (which might also be driven magnetically) has at least a moderately relativistic speed ($\sim 0.1 - 1c$).

(ii) The MHD acceleration model entails a high ($\gtrsim 50\%$) asymptotic conversion efficiency of injected magnetic and thermal energy into bulk kinetic energy for effectively confined flows. If the initial magnetization is of the same order as that of the inferred Lorentz factor of a GRB jet, $\sigma_0 \sim 10^2 - 10^3$, the energy conversion can be attained on

a spatial scale that is smaller than the indicated size of the prompt emission region. The model is then compatible with the internal-shocks scenario for GRBs. For a much higher initial magnetization the jet remains Poynting flux-dominated on these scales and the prompt emission has to be attributed to direct magnetic energy dissipation, as in the magnetodynamics scenario. A full treatment of the dynamics of such jets in the context of MHD would require taking account of the acceleration induced by the field-dissipation process and the use of a non-ideal, relativistic-MHD code.

(iii) We have found that the MHD jet model places a strong constraint on the product of the Lorentz factor and the half-opening angle of the streamline in the asymptotic regime of the main acceleration region: $\Gamma\theta_v \simeq 1$ along paraboloidal streamlines $z \propto r^b$ when $b \leq 2$ (but b not too close to 1), and $\Gamma\theta_v \propto z^{-(1-2/b)}$ (and thus attaining even smaller values at the end of the main acceleration phase) when $b > 2$. This feature is unique to the ideal MHD mechanism and could potentially serve to distinguish it from alternative models, notably the classical fireball scenario (in which $\Gamma\theta_v$ is envisioned to be $\gg 1$ at the end of the acceleration region). In particular, this property implies that, if long/soft GRB jets with $\Gamma \gtrsim 100$ are magnetically accelerated, they must be collimated to $\theta_v \lesssim 1^\circ$. This result is consistent with one of the interpretations of the prompt emission “tails” discovered by *Swift*, although this is not the only possible explanation of a very small collimation angle. This relationship also indicates that the γ -ray emitting outflow component might exhibit a panchromatic jet break (corresponding to $\Gamma\theta_v \simeq 1$ decreasing from a value > 1 to a value < 1) soon after it enters the afterglow phase, although in principle no such break need to occur (corresponding to cases where this product is < 1 at the end of the acceleration zone). A later jet break could potentially be seen if the outflow has more than one kinematic component.

(iv) The magnetic acceleration model also makes specific predictions about the angular distributions of the terminal Lorentz factor and of the kinetic and total energy per unit solid angle across the jet, which can be probed by a variety of observations. These distributions depend on the magnetization profile and the thermal energy content of the jet at the inlet boundary, which could in principle be constrained by the observations. A general characteristic of this model is that $\Gamma_\infty(\theta)$ decreases with decreasing polar angle θ near the symmetry axis.

Although our analytic scalings have been derived in the limit where the jet is in the force-free regime, we emphasize that key parameters of interest for astrophysical applications — including the jet velocity and the magnetic-to-kinetic energy conversion efficiency — could have only been obtained within the magnetohydrodynamics formalism that we adopted and not in the magnetodynamics (or force-free electrodynamics) approximation adopted in other recent semi-analytic and numerical investigations. Another point worth emphasizing is that the acceleration mechanism investigated in this paper is identical to that considered in paper I. Our results are consistent with the view that the main difference between “superluminal” AGN jets and GRB jets is that the latter outflows have a higher initial magnetization (and possibly also a higher initial enthalpy), which leads to their correspondingly higher terminal Lorentz fac-

tors. If this picture is correct, one could use observations of AGN and GRB sources to deduce complementary aspects of the same basic phenomenon. For example, one could take advantage of the fact that the acceleration region in AGN jets is potentially resolvable by radio interferometry to probe the details of the acceleration process; one could then consider the implications to GRB jets, which are not directly accessible to such observations.

ACKNOWLEDGMENTS

This research was funded by PPARC under the rolling grant “Theoretical Astrophysics in Leeds” (SSK and MVB). NV acknowledges partial support by the Special Account for Research Grants of the National and Kapodistrian University of Athens. AK was partially supported by a NASA Theoretical Astrophysics Program grant. We thank Vasily Beskin for many helpful comments on the magnetic acceleration mechanism and Jonathan Granot for useful discussions of GRB issues.

REFERENCES

- Barkov M. V., Komissarov S. S., 2008, MNRAS, 385, L28
 Barzilay Y., Levinson A., 2008, New Astr., 13, 386
 Begelman M. C., Li Z.-Y., 1994, ApJ, 326, 269
 Berger E., Kulkarni S. R., Frail D. A., 2003, ApJ, 590, 379
 Berger E., et al., 2003, Nature, 426, 154
 Beskin V. S., Kuznetsova I. V., Rafikov R. R., 1998, MNRAS, 299, 341
 Beskin V. S., Malyshev L. M., 2000, Astronomy Letters, 26, 208
 Beskin V. S., Nokhrina E. E., 2006, MNRAS, 367, 375
 Begelman M. C., Blandford R. D., Rees M. J., 1984, Rev. Mod. Phys., 56, 255
 Blandford R. D., 1976, MNRAS, 176, 465
 Blandford R. D., 2002, in Gilfanov M., et al., eds, Light-houses of the Universe. Springer-Verlag, Berlin, p. 381
 Blandford R. D., Payne D. G., 1982, MNRAS, 199, 883
 Bogovalov S. V., 1995, Astronomy Letters, 21, 565
 Bromberg O., Levinson A., 2007, ApJ, 671, 678
 Bucciantini N., Quataert E., Arons J., Metzger B. B., Thompson T. A., 2008, MNRAS, 383, 25
 Chiueh T., Li Z.-Y., Begelman M. C., 1991, ApJ, 377, 462
 Chiueh T., Li Z.-Y., Begelman M. C., 1998, ApJ, 505, 835
 Contopoulos J., 1994, ApJ, 432, 508
 Contopoulos I., Kazanas D., 2002, ApJ, 566, 336
 Drenkhahn G., 2002, A&A, 387, 714
 Drenkhahn G., Spruit H. C., 2002, A&A, 391, 1141
 Di Matteo T., Perna R., Narayan R., 2002, ApJ, 579, 706
 Eichler D., Levinson A., 2004, ApJ, 614, L13
 Frail D. A., Soderberg A. M., Kulkarni S. R., Berger E., Yost S., Fox D. W., Harrison F. A., 2005, ApJ, 619, 994
 Fuller G. M., Pruet J., Abazajian K., 2000, Phys. Rev. Lett., 85, 2673
 Genet F., Daigne F., Mochkovitch R., 2007, MNRAS, 381, 732
 Granot J., 2005, ApJ, 631, 1022
 Granot J., Königl A., Piran T., 2006, MNRAS, 370, 1946

Kamble A., Misra K., Bhattacharya D., Sagar R., 2008, MNRAS in press (arXiv:0806.4270)
 Katz J. I., 1997, ApJ, 490, 633
 Kluźniak W., Ruderman M., 1998, ApJ, 505, L113
 Kobayashi S., Zhang B., 2007, ApJ, 655, 973
 Komissarov S. S., 1999a, MNRAS, 303, 343
 Komissarov S. S., 1999b, MNRAS, 308, 1069
 Komissarov S. S., 2004, MNRAS, 350, 1431
 Komissarov S. S., Barkov M. V., Vlahakis N., Königl A., 2007, MNRAS, 380, 51 (Paper I)
 Komissarov S. S., Barkov M. V., 2007, MNRAS, 382, 1089
 Komissarov S. S., Lyubarsky Y. E., 2004, MNRAS, 349, 779
 Kumar P., et al., 2007, MNRAS, 376, L57
 Kumar P., Piran T., ApJ, 535, 152
 Lazzati D., Begelman, M. C., 2005, ApJ, 629, 903
 Levinson A., 2006, ApJ, 648, 510
 Levinson A., Eichler D., 1993, ApJ, 418, 386
 Levinson A., Eichler D., 2000, Phys. Rev. Lett., 85, 236
 Levinson A., Eichler D., 2003, ApJ, 594, L19
 Li Z.-Y., Chiueh T., Begelman M. C., 1992, ApJ, 394, 459
 Liang E.-W., Racusin J. L., Zhang B., Zhang B.-B., Burrows D. N., 2008, ApJ, 675, 528
 Liang E., Zhang B., 2005, ApJ, 633, 611
 Lithwick Y., Sari, R., 2001, ApJ, 555, 540
 Lyutikov M., 2006a, MNRAS, 369, L5
 Lyutikov M., 2006b, New J. Phys., 8, 119
 Lyubarsky Y., Eichler D., 2001, ApJ, 562, 494
 McKinney J. C., 2006, MNRAS, 368, 1561
 Mészáros P., 2006, Rep. Prog. Phys., 69, 2259
 Mészáros P., Rees M. J., 1997, ApJ, 482, L29
 Morsony B. J., Lazzati D., Begelman M. C., 2007, ApJ, 665, 569
 Nakar E., 2007, Phys. Rep., 442, 166
 Nakar E., Granot J., Guetta D., 2004, ApJ, 606, L37
 Nakar E., Piran T., 2003, New Astr., 8, 141
 Narayan R., McKinney J. C., Farmer A. J., 2007, MNRAS, 375, 548
 Okamoto I., 2002, ApJ, 573, L31
 Paczyński B., Wiita P., 1980, Å, 88, 23
 Panaitescu A., 2007, MNRAS, 379, 331
 Peng F., Königl A., Granot J., 2005, ApJ, 626, 966
 Piran T., 2005, Rev. Mod. Phys., 76, 1143
 Popham R., Woosley S. E., Fryer C., 1999, ApJ, 518, 356
 Proga D., MacFadyen A. I., Armitage P. J., Begelman M. C., 2003, ApJ, 629, 397
 Ramirez-Ruiz E., Celotti A., Rees M. J., 2002, MNRAS, 337, 1349
 Rhoads J. E., 1999, ApJ, 525, 737
 Rossi E., Lazzati D., Rees M. J., 2002, MNRAS, 332, 945
 Sari R., Piran T., Halpern J. P., 1999, ApJ, 519, L17
 Tchekhovskoy A., McKinney J. C., Narayan R., 2008, MNRAS, 388, 551
 Thompson C., 1994, MNRAS, 270, 480
 Tomimatsu A., Takahashi M., 2003, ApJ, 592, 321
 Uhm Z. L., Beloborodov A. M., 2007, ApJ, 665, L93
 Usov V. V., 1992, Nature, 357, 472
 Vlahakis N., 2004a, ApJ, 600, 324
 Vlahakis N., 2004b, Ap&SS, 293, 67
 Vlahakis N., Königl A., 2001, ApJ, 563, L129
 Vlahakis N., Königl A., 2003a, ApJ, 596, 1080
 Vlahakis N., Königl A., 2003b, ApJ, 596, 1104

Vlahakis N., Königl A., 2004, ApJ, 605, 656
 Vlahakis N., Peng F., Königl A., 2003, ApJ, 594, L23
 Vlahakis N., Tsinganos K., Sauty C., Trussoni E., 2000, MNRAS, 318, 417
 Zakamska N. L., Begelman M. C., Blandford R. D., 2008, ApJ, 679, 990
 Zhang B., 2007, Chin. J. Astron. Astrophys., 7, 1

APPENDIX A: SOLUTIONS OF EQUATION (52)

In Section 5.3 we considered the dependence of the jet boundary shape on the external pressure distribution, and we derived a second-order ordinary differential equation (equation 52) that expresses this dependence in the asymptotic regime of the main magnetic acceleration region for the case where the external pressure scales as $p_{\text{ext}} \propto z^{-\alpha}$. For convenience, we reproduce this equation here, keeping the original notation:

$$\frac{d^2x}{dZ^2} + C \frac{x}{Z^\alpha} - \frac{1}{x^3} = 0, \quad (\text{A1})$$

where C is a constant of the order of 1 (equation 49). In Section 5.3 we obtained solutions for this equation after making a power-law ansatz for $x(Z)$ (equation 53). In this appendix we consider general solutions of this equation without assuming from the start that they have a power-law form.

A1 $\alpha > 2$

One can identify three different regimes in this case.

A1.1 $2 < \alpha < 4$

When $\alpha < 4$ the ratio of the second (electromagnetic) to the third (centrifugal) terms on the left-hand side of equation (A1) diverges as $Z \rightarrow \infty$, and one can therefore neglect the centrifugal term in the asymptotic regime (as we also inferred in Section 5.3.1). Changing variables to

$$y \equiv \frac{\sqrt{C}}{|1 - \alpha/2|} Z^{1 - \alpha/2}, \quad f(y) \equiv \frac{x}{Z^{1/2}}, \quad (\text{A2})$$

this equation can then be written as

$$y^2 \frac{d^2f}{dy^2} + y \frac{df}{dy} + \left[y^2 - \left(\frac{1}{|2 - \alpha|} \right)^2 \right] f = 0, \quad (\text{A3})$$

whose solution is

$$f(y) = C_1 J_{1/|2 - \alpha|}(y) + C_2 Y_{1/|2 - \alpha|}(y). \quad (\text{A4})$$

For $\alpha > 2$ we have $1 - \alpha/2 < 0$, so the limit $Z \rightarrow \infty$ corresponds to $y \rightarrow 0$, in which case $J_\nu(y) \approx y^\nu$ and $Y_\nu(y) \approx 1/y^\nu$. Thus the term involving the Neumann function $Y_\nu(y)$ dominates, implying an asymptotic solution $f(y) \approx C_2/y^{1/(\alpha-2)}$, or, using the definition of y (equation A2),

$$r \approx C_2 z. \quad (\text{A5})$$

Thus, the solution is essentially paraboloidal (concave) with conical asymptotes.

A1.2 $\alpha = 4$

Changing the variable $x(Z)$ to $g(Z) \equiv x/Z$, equation (A1) becomes

$$Z^2 \frac{d^2 g}{dZ^2} + 2Z \frac{dg}{dZ} + \frac{Cg - 1/g^3}{Z^2} = 0. \quad (\text{A6})$$

This equation has an exact solution, $g = \text{const} = C^{-1/4}$, representing a flow that is conical from the start, $Z = C^{1/4}x$ (as we already found in Section 5.3.1), and in which the electromagnetic and centrifugal forces have comparable contributions.

A1.3 $\alpha > 4$

When $\alpha > 4$ the ratio of the third (centrifugal) to the second (electromagnetic) terms on the left-hand side of equation (A1) diverges as $Z \rightarrow \infty$, and one can therefore neglect the electromagnetic term in the asymptotic regime (as we also inferred in Section 5.3.1). Without this term, equation (A1) becomes

$$\frac{dx^2}{dZ^2} = \frac{1}{x^3}. \quad (\text{A7})$$

Multiplying by $2dx/dZ$, this equation can be integrated to give

$$\left(\frac{dx}{dZ}\right)^2 + \frac{1}{x^2} = \frac{1}{D}, \quad (\text{A8})$$

where D is a constant of integration. Equation (A8) can be further integrated to yield

$$\frac{x^2}{D} - \frac{(Z - Z_0)^2}{D^2} = 1, \quad (\text{A9})$$

where Z_0 is another constant of integration. Equation (A9) explicitly shows that the jet assumes a hyperboloidal shape in this case, with the asymptotes again being conical.

A2 $\alpha = 2$

Changing variables to $f \equiv x/Z^{1/2}$ (as in equation A2) and $q \equiv \ln Z$, equation (A1) becomes in this case

$$\frac{d^2 f}{dq^2} = \left(\frac{1}{4} - C\right) f + \frac{1}{f^3}. \quad (\text{A10})$$

One obvious solution is $f = \text{const}$, with $f^{-1/4} = C - 1/4$, or $Z = \sqrt{C - 1/4} x^2$. This solution is real only for $C > 1/4$.

For $df/dq \neq 0$, equation (A10) can be multiplied by $2df/dq$ and rewritten as

$$\frac{d}{dq} \left[\left(\frac{df}{dq}\right)^2 + \left(C - \frac{1}{4}\right) f^2 + \frac{1}{f^2} \right] = 0, \quad (\text{A11})$$

or, with $u \equiv f^2$,

$$\left(\frac{du}{dq}\right)^2 = (1 - 4C)u^2 + 4Eu - 4, \quad (\text{A12})$$

where E is a constant of integration. This can be integrated to give

$$\pm 2 \int dq = \int \frac{du}{\sqrt{\left(\frac{1}{4} - C\right) u^2 + Eu - 1}} =$$

$$\left\{ \begin{array}{l} \frac{\ln\left(\frac{E/2}{\frac{1}{4}-C} + u + \sqrt{u^2 + \frac{Eu-1}{\frac{1}{4}-C}}\right)}{\sqrt{\frac{1}{4}-C}}, C < \frac{1}{4} \\ 2\frac{\sqrt{Eu-1}}{E}, C = \frac{1}{4} \\ \frac{-1}{\sqrt{C-\frac{1}{4}}} \arctan \frac{\frac{E/2}{C-\frac{1}{4}} - u}{\sqrt{-u^2 + \frac{Eu-1}{C-\frac{1}{4}}}}, C > \frac{1}{4}. \end{array} \right. \quad (\text{A13})$$

The quantity inside the square root in the integrand must be positive in the asymptotic regime. This implies that u cannot tend to zero as $Z \rightarrow \infty$, and so it either tends to a constant or to ∞ . The first option is unacceptable as it gives $q = \text{const} \Leftrightarrow Z = \text{const}$. Thus, we must have $u \rightarrow \infty$ as $Z \rightarrow \infty$. Since $u = f^2 = x^2/Z$, this means that the shape is $Z \propto x^b$ with $b < 2$. The dominant term inside the square root in the integrand when $Z \rightarrow \infty$ is the first one, which implies $C \leq 1/4$ (and hence that the $C > 1/4$ solution branch of equation A13 is not physical).

For $C = 1/4$, equation (A13) gives $x = Z^{1/2} \sqrt{1/E + E [\ln(Z/Z_0)]^2}$, or, keeping only the dominant terms, $x = Z^{1/2}(C_1 + C_2 \ln Z)$. In view of the requirement $u = x^2/Z \rightarrow \infty$ as $Z \rightarrow \infty$ derived above, one must keep the logarithmic term in this solution (i.e. $C_2 \neq 0$). We also keep the other term in this solution, which may be needed to match to the conditions at the base of the flow (see Section 5.3.2). Note that this solution could not be derived from the ansatz employed in Section 5.3 since it does not have a pure power-law form.

For $C < 1/4$, equation (A13) gives (keeping only the dominant terms) $x = C_1 Z^{\frac{1}{2} \pm \frac{1}{2} \sqrt{1-4C}}$. Since, as we found above, the exponent b in $Z \propto x^b$ must be < 2 the only acceptable solution is $x = C_1 Z^{\frac{1}{2} + \frac{1}{2} \sqrt{1-4C}}$.

Summarizing,

for $C > 1/4$, $Z = \sqrt{C - 1/4} x^2$,

for $C = 1/4$, $x = Z^{1/2}(C_1 + C_2 \ln Z)$ with $C_2 \neq 0$, and

for $C < 1/4$, $x = C_1 Z^{\frac{1}{2} + \frac{1}{2} \sqrt{1-4C}}$.

The first case ($C > 1/4$) represents a balance between the poloidal curvature, electromagnetic and centrifugal terms in equation (A1), whereas in the last two cases ($C \leq 1/4$) only the poloidal curvature and electromagnetic terms play a role.

A3 $\alpha < 2$

As discussed in Section 5.3.3, in this case the poloidal curvature term — the first term on the left-hand side of equation (A1) — can be neglected. The power-law form for $x(Z)$ given in the main text is then an exact solution of this equation.